

Coupling–energy driven pumping through quantum dots: the role of coherences

Lukas Litzba,^{1,*} Gernot Schaller,² Jürgen König,¹ and Nikodem Szpak¹

¹*Fakultät für Physik and CENIDE, Universität Duisburg–Essen, Lotharstraße 1, Duisburg 47057, Germany*

²*Helmholtz–Zentrum Dresden–Rossendorf, Bautzner Landstraße 400, 01328 Dresden, Germany*

(Dated: February 27, 2026)

We study the impact of off–resonant tunneling and coherences on the electron pumping through quantum dots. Thereby, we focus on two electron–pump setups where lowest–order tunneling processes are suppressed and the pump is exclusively driven by modulations of the coupling energy. The first setup is driven by switching on and off the couplings between the quantum dot and the leads, while the second setup employs measurements of the dot occupation. We derive exact solutions for arbitrarily strong tunnel couplings in the absence of Coulomb interaction, identify parameter regimes with optimal pumping currents or optimal energy efficiency, and discuss similarities between both pumping mechanisms.

I. INTRODUCTION

Modern miniaturized devices laying the foundations for quantum technologies are typically operating at the nanoscale where quantum effects begin to dominate. A major challenge is to understand how quantum properties modify their operation and efficiency [1–20], compared to their classical counterparts. From a theoretical point of view, such devices can be modeled as open quantum systems coupled to an environment. Often, the interaction between the quantum system and the environment is assumed to be weak and accounted for to lowest–order perturbation theory only. That goes hand in hand with neglecting the coupling energy of the interaction. However, beyond the weak–coupling regime, the coupling energies and higher–order interaction processes become relevant [21–31]. How they alter the properties and performance of the devices is currently a topic of intensive research [1–14, 31–38]. In contrast to previous works, where the impact of the coupling energy was treated on top of the lowest–order coupling processes, we focus here on devices that are enabled and operated exclusively by the coupling energy and the dynamical modulation of the associated coherences. They rely on the observation that *the destruction of quantum coherence can pump energy into a system* [21]. In particular, repeated externally induced decoherence operations can continuously pump energy into the device by driving off–resonant tunneling (schematically shown in Figure 1). Based on these repeated external operations leading to decoherence¹, we consider two pumping schemes of a device that pump electrons against an applied voltage: For one of them, the coupling between the open system and the environment is periodically switched on and off (cf. Section III), while the other one is based on measurement–induced ef-

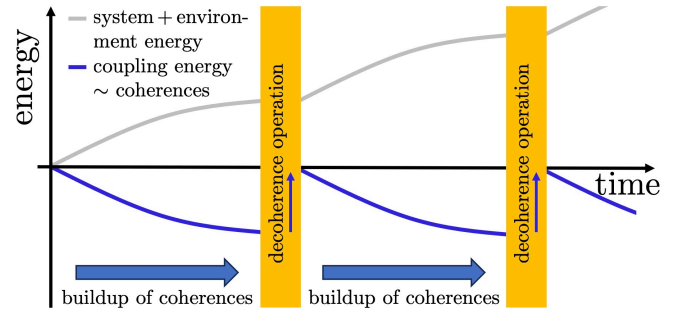


FIG. 1. Sketch of an open quantum system subject to repeated interventions erasing the system–environment coherences and thereby the coupling energy. In between, coherences may rebuild and the energy of system plus environment may increase on the cost of the coupling energy.

fects similar to the anti–Zeno effect [41–44] (cf. Section IV).

The device we consider consists of a quantum dot (QD), often described as an *artificial atom*, placed between two fermionic baths. We consider the energy levels of the QD to be time–independent and higher than the chemical potentials of the baths. This ensures that lowest–order and resonant tunneling processes between the baths are blocked and only off–resonant tunneling processes related to the QD–bath coupling are relevant for the transport. In contrast, in common experimental realizations [45–61]², pumping is achieved by varying the energy levels of the QD over time, as in an elevator, and involves primarily lowest–order and resonant tunneling processes.

In general, electron pumps have also been considered theoretically [16, 35, 62–74], have important applications as single–electron sources in the field of metrology [57], and are often treated in the weak–coupling

* lukas.litzba@uni-due.de

¹ In contrast to the concept of *coherences as a resource* [39, 40], in which coherences are used as a fuel to extract energy from the bath, here we induce decays of the coherences between the bath and the QD. Such decays increase the coupling energy and finally the energy of the QD and the bath.

² In some experiments, only the gate voltage corresponding to the coupling strength is varied. In these cases, however, this results in an additional shift of the onsite potential of the QD and thus in an elevator–like behavior.

limit. However, for strong couplings or for structured baths, higher-order or off-resonant tunneling processes and non-Markovian effects become also important [16]. In this context, our focus on processes driven by the coupling energy itself is of particular interest because the work required to decouple QD and bath, or more generally, the work required to decouple the environment and the working medium of a thermodynamic machine, is a key cause of the reduction in efficiency of these devices at the nanoscale [1–5] — in particular, in the strong-coupling regime. Furthermore, performing local measurements on the device is influenced by the coupling energy which must be taken into account when studying measurement-induced pumping with feedback control, e.g. quantum Maxwell demons [34–37]. In addition, it is possible to drive an engine only by the work performed by the measurement process itself [74, 75]. In our work (second pumping scheme), we focus on measurement-induced pumping without feedback control by considering highly-structured baths.

For both pumping schemes, the structures of the baths and related non-Markovian effects [76] have significant influence on the efficiency. In particular, we find that non-Markovian effects can boost the performance of the electron pump which is already known for other engines [2–10, 18]. In contrast to the adiabatic regime, where the transferred charge per cycle is independent of the driving frequency for the coupling- and decoupling-induced pumping (first pumping scheme) [63, 66], we operate in a deeply non-adiabatic regime.

We consider the QD in the absence of Coulomb interaction. This allows us to handle arbitrarily strong coupling and non-Markovian effects because then an exact solution can be directly obtained by the extension of the exact Heisenberg equation and Laplace-transform technique [77] to time-dependent Hamiltonians.

The paper is structured as follows. In Section II, we explain the model that describes the QD placed between two fermionic baths. In Section III, we consider the coupling- and decoupling-induced pumping where in the following we will label it as pumping scheme 1. First, we discuss the slow pumping regime in Section III A. In particular, we identify a high energy efficiency regime and discuss efficiency improvements for finite cycle durations in a second step (cf. Section III B). In Section IV, we consider measurement-induced pumping, where in the following we will label it as pumping scheme 2. We study periodically repeated projective measurements (cf. Section IV A), but also weak continuous measurement via a single-electron transistor (SET) (cf. Section IV B). In addition, we compare the results for pumping scheme 1 with those of pumping scheme 2. We demonstrate that both pumps are based on destruction of QD-bath coherences and show quantitative and qualitative similarities (cf. Section V).

II. MODEL

Throughout this paper, we consider a quantum dot (QD) placed between two fermionic baths, as sketched in Figure 2 (left).

A. Hamiltonian

The starting point for our calculations is the single-impurity tunneling Hamiltonian

$$H(t) = H_S + H_C(t) + H_B, \quad (1)$$

in which $H_S = \varepsilon c^\dagger c$ with creation and annihilation operators c^\dagger and c describes the open quantum system consisting of a single QD-orbital of energy ε that is tunnel coupled to two fermionic baths modeled by $H_B = \sum_{\nu,k} \varepsilon_{\nu,k} a_{\nu,k}^\dagger a_{\nu,k}$, where $\nu = 1, 2$ is the bath index and $\varepsilon_{\nu,k}$ the dispersion relation for states labeled by k in bath ν . We assume the baths to be infinitely large and initially given by the tensor product of the Gibbs states $\rho_{B,\nu}(0) \sim \exp\left(-\beta \sum_k (\varepsilon_{\nu,k} - \mu_\nu) a_{\nu,k}^\dagger a_{\nu,k}\right)$ with inverse temperature³ β and with chemical potentials μ_ν . Without loss of generality, we consider $\mu_1 \leq \mu_2$, define the voltage $V = \mu_2 - \mu_1$ and choose $\mu_1 = 0$ as the energy reference.

In the following, we focus on the low-temperature limit, $\beta \rightarrow \infty$, and assume the energy of the QD orbital to lie above the chemical potentials of both leads, $\varepsilon > \mu_2$. Thereby, we ensure that resonant electron transport is suppressed.

The tunnel coupling between QD and bath is described by the Hamiltonian

$$H_C(t) = \sum_{\nu,k} \left(\gamma_{\nu,k}(t) a_{\nu,k}^\dagger c + \text{h.c.} \right). \quad (2)$$

In contrast to H_S and H_B , we permit time-dependent $H_C(t)$ through the tunnel matrix elements $\gamma_{\nu,k}(t) \equiv \gamma_{\nu,k} g_\nu(t)$, in which $g_\nu(t)$ accounts for the possibility of time-variable strength of the tunnel coupling between the QD orbital and bath ν . We assume that the associated spectral coupling-density

$$\begin{aligned} \Gamma_\nu(\omega, t) &= 2\pi \sum_k |\gamma_{\nu,k}(t)|^2 \delta(\omega - \varepsilon_{\nu,k}) \\ &= g_\nu^2(t) \frac{\Gamma_\nu \Delta_\nu^2}{(\omega - \omega_\nu)^2 + \Delta_\nu^2} \end{aligned} \quad (3)$$

has a Lorentzian shape with center position ω_ν , width Δ_ν and the strength Γ_ν (for $g_\nu(t) \equiv 1$), i.e., we use these three parameters instead of the infinitely many tunnel matrix elements $\gamma_{\nu,k}$ to characterize the tunnel coupling to bath ν .

³ We set both bath temperatures equal for simplicity, however, they can be generally also treated as different.

B. Reaction-coordinate mapping

The total Hamiltonian H (cf. Eq. (1)) is only bilinear in the fermionic operators. If, in addition, the Hamiltonian is also time independent then an exact solution is available by solving the Heisenberg equations of motion with the help of the Laplace transform [77]. A direct application of this technique for our purpose is hindered by the time dependence of the coupling term $H_C(t)$. To circumvent this problem, we perform as a first step a fermionic reaction-coordinate mapping [78] for each of the baths, as visualized in Figure 2. For each bath a unitary transformation is applied such that the QD orbital is no longer coupled to all the states of a given bath, but rather to one state only, which is referred to as the reaction coordinate (RC). The coupling Hamiltonian H_C (cf. Eq. (2)) together with a Lorentzian spectral coupling-density of width Δ_ν and strength Γ_ν yields the creation operator

$$r_\nu^\dagger = \sqrt{\frac{2}{\Delta_\nu \Gamma_\nu}} \sum_k \gamma_{\nu,k} a_{\nu,k}^\dagger \quad (4)$$

for the reaction coordinate of bath ν , where the prefactor ensures the normalization condition, and the reaction-coordinate energy is given by the center ω_ν of the Lorentzian (cf. Eq. (3)). The remaining part of the bath Hilbert space is re-diagonalized, which leads to new bath-state creation operators $\tilde{a}_{\nu,k}^\dagger$ that couple to the reaction coordinate with new matrix elements $\tilde{\gamma}_{\nu,k}$. As a result, the reaction-coordinate mapping rewrites the total Hamiltonian in the form

$$H(t) = \tilde{H}_S(t) + \tilde{H}_C + \tilde{H}_B. \quad (5)$$

The new super-system Hamiltonian

$$\tilde{H}_S(t) = \varepsilon c^\dagger c + \sum_\nu \left[\omega_\nu r_\nu^\dagger r_\nu + g_\nu(t) \sqrt{\frac{\Gamma_\nu \Delta_\nu}{2}} (r_\nu^\dagger c + \text{h.c.}) \right] \quad (6)$$

now includes not only the QD level but also the two reaction coordinates. It becomes time-dependent through the variation of the coupling strengths $g_\nu(t)$. The new coupling Hamiltonian \tilde{H}_C is now independent of time. The couplings between new super-system and new baths are once more accounted for by a spectral coupling-density. As has been shown in Ref. [78], the Lorentzian shape of the $\Gamma_\nu(\omega, t)$ of the original model yields a constant, i.e., time- and energy-independent, spectral coupling-density $\tilde{\Gamma}_\nu = 2\Delta_\nu$. Its strength is given by twice the width of the original Lorentzian. The originally structured bath coupling is, thus, mapped onto a structureless one, i.e., it fulfills the wideband condition, see Figure 2. The time independence of $\tilde{\Gamma}_\nu$ makes it possible to extend, in a straightforward way, the Laplace-transform technique of Ref. [77] to the system of consideration in the present paper, see Appendix A.

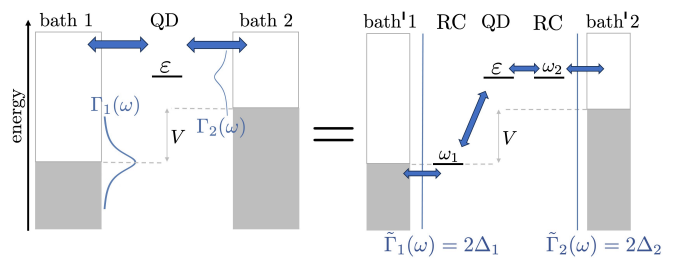


FIG. 2. Schematic visualization of the fermionic reaction-coordinate mapping [78]: A quantum dot (QD) coupled to two Lorentzian shaped baths is equivalent to the situation where the QD is coupled to two reaction-coordinates (RC) that are coupled to two new baths with wideband spectral-coupling densities.

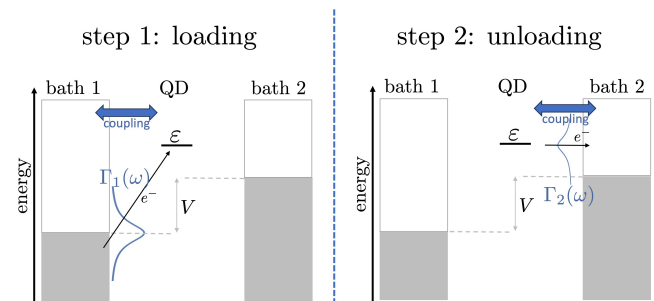


FIG. 3. Schematic visualization of the functionality (step 1 and step 2 form one pumping cycle) of pumping scheme 1: The pump consists of a quantum dot (QD) that has a time-independent onsite potential ε and is located between two baths at zero temperature. The difference of the chemical potentials μ_1 and μ_2 of the baths is given by V . Here, the pumping results only from the coupling and decoupling processes with the baths. In order to study non-Markovian effects, we consider structured baths with Lorentzian shaped spectral densities $\Gamma_1(\omega)$, $\Gamma_2(\omega)$ [76].

III. PUMPING SCHEME 1

Both pumping schemes that we discuss in this paper rely, on the one hand, on the structured spectral coupling densities, characterized by the center positions ω_ν , widths Δ_ν and the strengths Γ_ν for bath $\nu = 1, 2$ and, on the other hand, on the alternation of formation and decay of coherences between the quantum dot (QD) and the baths.

In the first pumping scheme, this alternation is triggered by periodically switching on the coupling to one of the baths and simultaneously switching off the coupling to the other bath (cf. Figure 3). To be specific, we assume a stepwise⁴ switching between the QD being coupled to bath 1 (with duration t_1) and to bath 2 (with

⁴ For computational reasons, we only consider sharp step functions for $g_\nu(t)$, but it is not necessary for the pump effect itself. Thus, we are always in a non-adiabatic regime.

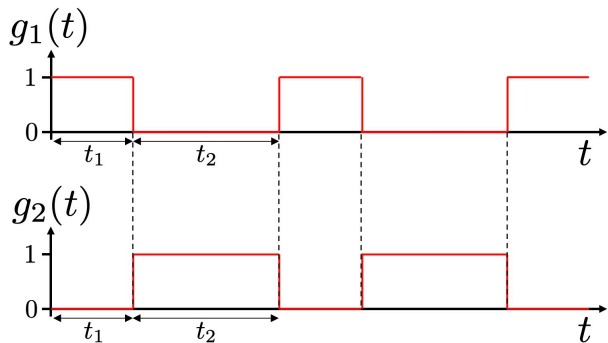


FIG. 4. The coupling function $g_\nu(t)$ for $\nu = 1, 2$ as a function of time t with the duration t_1 of step 1 and the duration t_2 of step 2. The functions fulfill the relation $g_1(t) = 1 - g_2(t)$.

duration t_2). This is described by the functions $g_\nu(t)$ as shown in Figure 4.

During step 1 and 2, charge can only be exchanged between the QD and bath 1 and 2, respectively. The average number of electrons pumped into bath 2 is, therefore, the QD occupation at the beginning minus the occupation at the end of step 2. This results in

$$N_{\text{pump}} = \langle n_{\text{QD}}(\ell t_1 + (\ell - 1)t_2) \rangle - \langle n_{\text{QD}}(\ell t_1 + \ell t_2) \rangle \quad (7)$$

for the ℓ -th cycle, and the corresponding averaged current is given by

$$I_{\text{pump}} = \frac{N_{\text{pump}}}{t_1 + t_2}. \quad (8)$$

A. Slow Pumping

In this section, we consider coupling periods t_1 and t_2 that are long enough for the device to reach the stationary state during each step (formally $t_1, t_2 \rightarrow \infty$). Here, after each step, the coherences between the QD and the previously uncoupled bath have completely decayed. This corresponds to the decoherence operation, mentioned in Figure 1, that drives off-resonant tunneling. In this case, the QD occupations entering Eq. (7) are the stationary ones, $\langle n_{\text{stat},1} \rangle$ and $\langle n_{\text{stat},2} \rangle$, for the QD being coupled to bath 1 or 2, respectively. The number of pumped charges per cycle is, then,

$$N_{\text{pump}} \approx \langle n_{\text{stat},1} \rangle - \langle n_{\text{stat},2} \rangle. \quad (9)$$

In the weak-coupling limit for both baths, the stationary QD occupations are both zero, because we consider zero bath temperatures and $\varepsilon > \mu_2 > \mu_1$. For stronger coupling, however, $\langle n_{\text{stat},1} \rangle$ and $\langle n_{\text{stat},2} \rangle$ are finite, given by

$$\langle n_{\text{stat},\nu} \rangle = \int_{-\infty}^{\mu_\nu} \frac{d\omega}{2\pi} \frac{\Gamma_\nu}{(\varepsilon - \omega)^2 + \left(\frac{\Gamma_\nu}{2} + \frac{(\varepsilon - \omega)(\omega - \mu_\nu)}{\Delta_\nu} \right)^2} \quad (10)$$

(cf. Appendix A 2) where the coupling strength Γ_ν can be interpreted as an effective broadening of the energy level. Thus, $\langle n_{\text{stat},\nu} \rangle$ increases for increasing coupling strength Γ_ν but decreases for increasing $\varepsilon - \mu_\nu$. This implies that for equally coupled baths, $\Gamma_1(\omega) = \Gamma_2(\omega)$, since $\varepsilon - \mu_1 > \varepsilon - \mu_2$, there will be no transport against the bias, $N_{\text{pump}} < 0$. However, if the coupling strength Γ_1 is sufficiently large compared to Γ_2 then $\langle n_{\text{stat},1} \rangle > \langle n_{\text{stat},2} \rangle$ is possible, such that electrons are pumped against the applied voltage, $N_{\text{pump}} > 0$.

As a further simplification, we consider an extremely weak coupling Γ_2 between the QD and the second bath, still respecting $\Gamma_2 t_2 \gg 1$, such that the QD is completely emptied after step 2. The number of pumped electrons is, then, given by

$$N_{\text{pump}} \approx \langle n_{\text{stat},1} \rangle, \quad (11)$$

i.e., the stationary QD occupation of step 1.

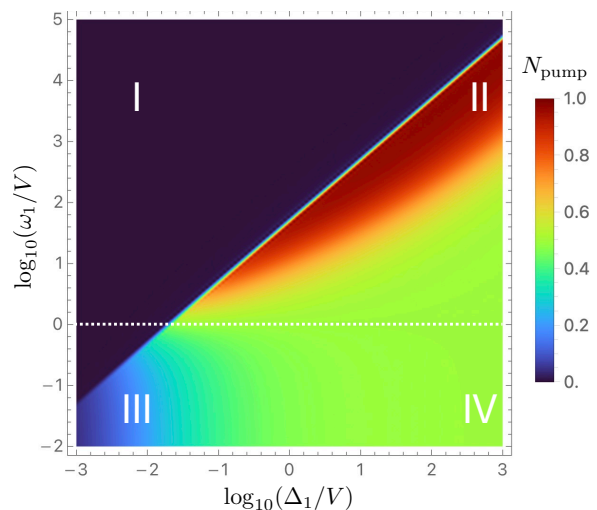


FIG. 5. Average number of electrons $N_{\text{pump}} \approx \langle n_{\text{stat},1} \rangle$ pumped during one cycle as a function of the width Δ_1 (logarithmic scale) and the peak position ω_1 (logarithmic scale) of the spectral coupling-density of the first bath in the slow-pumping regime, $t_1, t_2 \rightarrow \infty$. The QD-orbital energy $\varepsilon = V + 0^+$ is directly above the chemical potential of the second bath. The coupling with the first bath is $\Gamma_1 = 100V$ whereas the coupling with the second bath is chosen sufficiently weak (formally $\Gamma_2 \searrow 0$) such that the QD is completely emptied after step 2. Pumping is suppressed for $\omega_1 > \frac{\Delta_1 \Gamma_1}{2\varepsilon}$ (region I) and is largest in region II.

Figure 5 shows N_{pump} as a function of the width Δ_1 and the peak position ω_1 of the spectral coupling-density $\Gamma_1(\omega, t)$ with $\Gamma_1 = 100V$, obtained from the exact solution (cf. Eq. (10) and Appendix A 2). We find that N_{pump} strongly depends on Δ_1 and ω_1 . In particular, there is a line $\omega_1 = \frac{\Delta_1 \Gamma_1}{2\varepsilon}$, above which pumping is strongly suppressed (region I). Below this line (regions II-IV), pumping occurs. The dependence of N_{pump} on Δ_1 and ω_1 can be qualitatively understood in terms of

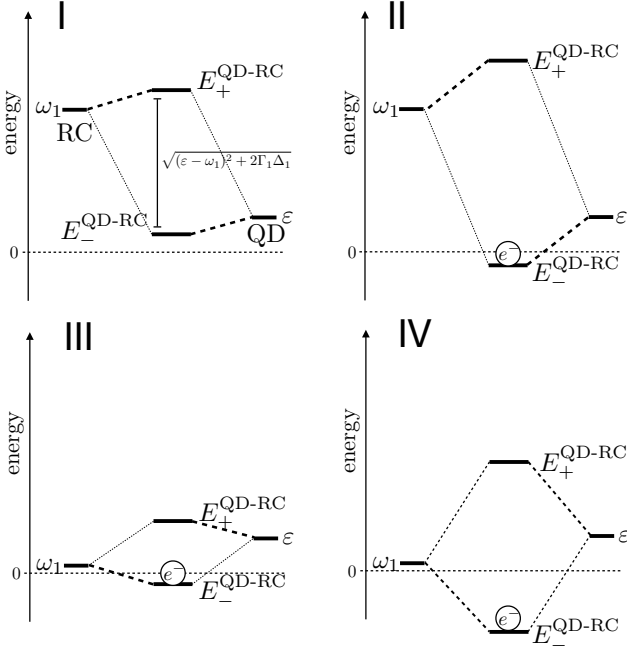


FIG. 6. Schematic visualization of the hybridized states that result from coupling the QD and the reaction coordinate (RC): Each graph (I–IV) shows the energy levels of the reaction coordinate ω_1 and of the QD ϵ in relation to the chemical potential $\mu_1 = 0$. In addition, the two energy levels $E_{\pm}^{\text{QD-RC}}$ of the hybridized states that result from the coupling between the QD and the reaction coordinate of the first reservoir during step 1 with level splitting $\sqrt{(\epsilon - \omega_1)^2 + 2\Gamma_1\Delta_1}$ are drawn between the energy levels of the reaction coordinate and the QD. Furthermore, the thickness of the dashed lines that connect the pure QD/reaction coordinate and the hybridized levels symbolize the corresponding overlaps between them. The graphs I–IV correspond to the regions I–IV in Figure 5. In region I ($\omega_1 > \frac{\Gamma_1\Delta_1}{2\epsilon}$), the lowest hybridized energy is larger than μ_1 and therefore this state will not be significantly occupied. In contrast, in regions II–IV, the lowest hybridized energy levels lie below μ_1 and these states will be predominantly occupied. Since the overlaps between the lower hybridized states and the QD are different, so are the occupations of the QD: In region II, large overlap $\Rightarrow \langle n_{\text{stat},1} \rangle \approx 1$; in region III, small overlap $\Rightarrow \langle n_{\text{stat},1} \rangle \approx 0$; in region IV, approximately equal overlap with QD and reaction coordinate $\Rightarrow \langle n_{\text{stat},1} \rangle \approx \frac{1}{2}$; dashed–white line in Figure 5 ($\omega_1 = \epsilon$), exactly equal overlap with QD and reaction coordinate $\Rightarrow \langle n_{\text{stat},1} \rangle = \frac{1}{2}$.

the energy ω_1 of the first reaction–coordinate, the energy ϵ of the QD level and their coupling $\sqrt{\Gamma_1\Delta_1}/2$. For this, we diagonalize the subspace of reaction–coordinate 1 and QD level to get two eigenstates with energies

$$E_{\pm}^{\text{QD-RC}} = \frac{\epsilon + \omega_1}{2} \pm \frac{1}{2}\sqrt{(\epsilon - \omega_1)^2 + 2\Gamma_1\Delta_1}. \quad (12)$$

For pumping, the state with the lower energy $E_-^{\text{QD-RC}}$ is relevant. It must be occupied and must have a large overlap with the bare QD level in order to maximize $\langle n_{\text{stat},1} \rangle$ and, therefore, also N_{pump} .

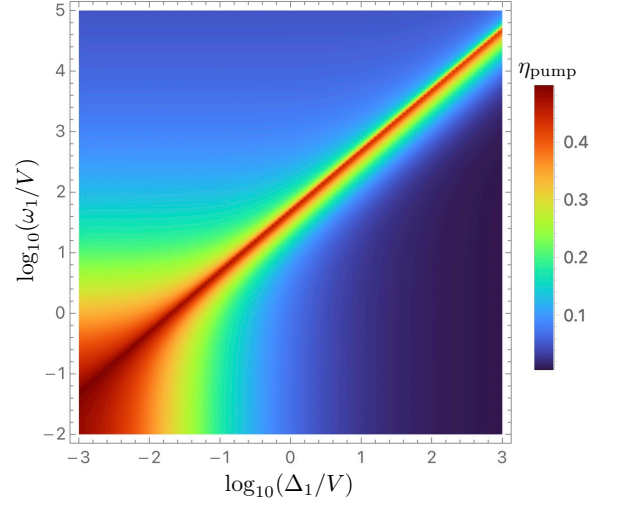


FIG. 7. The energy efficiency η_{pump} as a function of the width Δ_1 (logarithmic scale) and the peak position ω_1 (logarithmic scale) of the spectral coupling–density of the first bath. The parameters are the same as in Figure 5. In contrast to N_{pump} that vanishes for highly structured baths ($\Delta_1 \ll V$), the efficiency η_{pump} is optimized in this regime for $\omega_1 \ll V$. For $\omega_1 = \frac{\Delta_1\Gamma_1}{2\epsilon}$, η_{pump} shows a special behavior analogous to N_{pump} and reaches large values compared to η_{pump} for the surrounding parameters. Moreover, there is a non–zero efficiency for $\omega_1 > \frac{\Delta_1\Gamma_1}{2\epsilon}$. At first glance, this is surprising because this is the non–pumping regime. However, there is a small N_{pump} and also a small performed work which leads to $\eta_{\text{pump}} > 0$.

In the following, we distinguish four regimes, as depicted in Figure 6. Region I is defined by $\omega_1 > \frac{\Gamma_1\Delta_1}{2\epsilon}$, for which the energy of the lower hybridized state lies above the chemical potential of bath 1, $E_-^{\text{QD-RC}} > 0$. In this case, the occupation of the hybridized level and, therefore, also N_{pump} is suppressed⁵.

A sizable occupation occurs only for $E_-^{\text{QD-RC}} < 0$, or, equivalently, $\frac{\Gamma_1\Delta_1}{2\epsilon} > \omega_1$ (regions II–IV). The largest overlap between the hybridized state and the bare QD level is achieved if the energy of reaction–coordinate 1 lies (in units of the coupling between the reaction coordinate and the QD level) well above the bare QD level, $\omega_1 - \epsilon \gg \sqrt{2\Gamma_1\Delta_1}$. This defines region II, for which the pumped charge per cycle becomes maximal, $N_{\text{pump}} \approx 1$. In regions III and IV, the energy ω_1 of the reaction coordinate lies below the QD level ϵ . For weak hybridization, $\sqrt{2\Gamma_1\Delta_1} \ll |\omega_1 - \epsilon|$ (region III), the overlap between the hybridized state and the QD is small, resulting in a small N_{pump} . Finally, for strong hybridization, $\sqrt{2\Gamma_1\Delta_1} \gg |\omega_1 - \epsilon|$ (region IV), the lower hybridized state is an antisymmetric superposition of the QD and the reaction coordinate, resulting in $N_{\text{pump}} \approx \frac{1}{2}$.

⁵ However, there will be a small but finite occupation because of off–resonant and higher–order tunneling processes.

The pumped charge per cycle is only one number that characterizes the electron pump. Another one is the energy efficiency η_{pump} . It quantifies which percentage of the work performed during the coupling and decoupling procedure is converted into the chemical energy gain of the second bath.

The work performed on the device by changing the coupling between QD and baths at time t is given by

$$W_C(t) = \langle H_C(t+0^+) \rangle - \langle H_C(t-0^+) \rangle \quad (13)$$

i.e., the change of the expectation value of the coupling Hamiltonian H_C at time t . The total net performed work during the ℓ -th cycle is, therefore, the sum $W_C(\ell t_1 + (\ell - 1)t_2) + W_C(\ell t_1 + \ell t_2)$ of the works performed during both switching processes. This yields, for the long-time limit, the energy efficiency

$$\eta_{\text{pump}} = \lim_{\ell \rightarrow \infty} \frac{N_{\text{pump}} V}{W_C(\ell t_1 + (\ell - 1)t_2) + W_C(\ell t_1 + \ell t_2)}, \quad (14)$$

since $N_{\text{pump}} V$ is the chemical energy gain per pumping cycle (cf. Figure 7).

While Eq. (14) is valid for arbitrary t_1 and t_2 , we show in Figure 7 the limit of slow pumping, $t_1, t_2 \rightarrow \infty$. In the wideband limit $\Delta_1 \rightarrow \infty$, excitations are generated all over the bath during the pumping process. This means that the performed work is mainly converted into excitations in the bath but not into the pumping of electrons. Therefore, η_{pump} vanishes even though N_{pump} can have a large value. In the opposite limit, $\Delta_1 \rightarrow 0$, effectively only one bath mode, the reaction coordinate, becomes excited during the pumping process. Here, the performed work splits half and half between excitations in the bath and pumping (cf. Appendix A 3), resulting in the maximally possible value $\eta_{\text{pump}} = \frac{1}{2}$ for slow pumping.

For finite values of t_1 and t_2 , i.e., beyond slow pumping, pumping-efficiency values higher than $\frac{1}{2}$ are possible. This we discuss in Section III B. The improved efficiency relies on non-Markovian effects for finite t_1 , t_2 and Γ_2 . There, we focus on structured baths with small Δ_1 , because, as we have seen above, in that case the work performed by switching the couplings is converted more efficiently into the chemical energy gain of the second bath. In addition, in this regime it is possible to study oscillations of N_{pump} as an indicator for the impact of coherences between the QD and the baths.

B. Improved efficiency in generic pumping

In the slow-pumping regime ($t_1, t_2 \rightarrow \infty$), described in Section III A, the coherence between the QD and the bath to which it is momentarily coupled has reached its stationary limit, and the coherence with the other bath has fully decayed. In the present section, we study the more complicated situation that the step durations t_1 and t_2 are kept finite, for which the time dependence of the coherence becomes important.

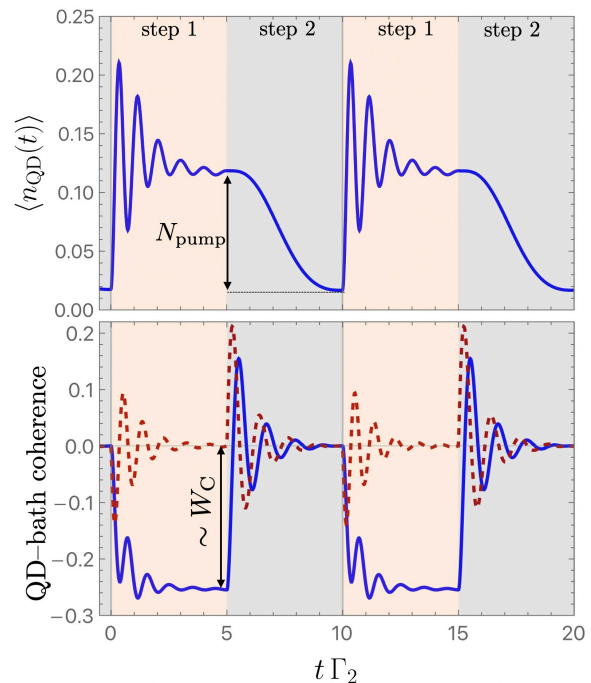


FIG. 8. The Figures show the particle number of the QD (top) and the collective coherence $\langle r_1^\dagger c \rangle$ between the QD and the first bath (cf. Eq. (4)) (bottom: blue–solid curve $\hat{=}$ real part; red–dashed curve $\hat{=}$ imaginary part) as functions of time t . Additionally, N_{pump} and W_C are shown in the plots. The durations of step 1 and step 2 are equal, $t_1 = t_2 = \frac{5}{\Gamma_2} = \frac{40}{V}$, and large compared to $\frac{1}{\Delta_1}$, $\frac{1}{\Delta_2}$, $\frac{1}{\Gamma_1}$ and $\frac{1}{\Gamma_2}$. Thus, the coherence $\langle r_1^\dagger c \rangle$ vanishes almost completely at the end of step 2. However, this is different for shorter t_2 (cf. Figure 10). The other parameters are given by $\Gamma_1 = \frac{5}{2}V$, $\Delta_1 = \frac{V}{2}$, $\Gamma_2 = \frac{1}{4}V$, $\Delta_2 = \frac{1}{8}V$, $\varepsilon = \frac{5}{4}V$, $\omega_1 = 0$ and $\omega_2 = \varepsilon$.

Strong non-Markovian effects such as oscillations of the QD occupation may appear⁶. As one result, one may achieve an improved energy efficiency η_{pump} for pumping.

The coherence between the QD and, say, bath 1 is quantitatively characterized by the expectation value $\langle r_1^\dagger c \rangle$ involving one operator for the QD and one for reaction-coordinate 1. In the presence of a tunneling coupling (i.e. during step 1), the real part of the coherence is related to the coupling energy

$$\langle H_C(t) \rangle = 2\sqrt{\frac{\Gamma_1 \Delta_1}{2}} \text{Re} \langle r_1^\dagger c \rangle, \quad (15)$$

while the imaginary part describes the current from bath

⁶ In general, oscillations can occur in Markovian systems, but for a single QD, oscillations in the occupation can be directly linked to information back-flow and thus to non-Markovian effects [79].

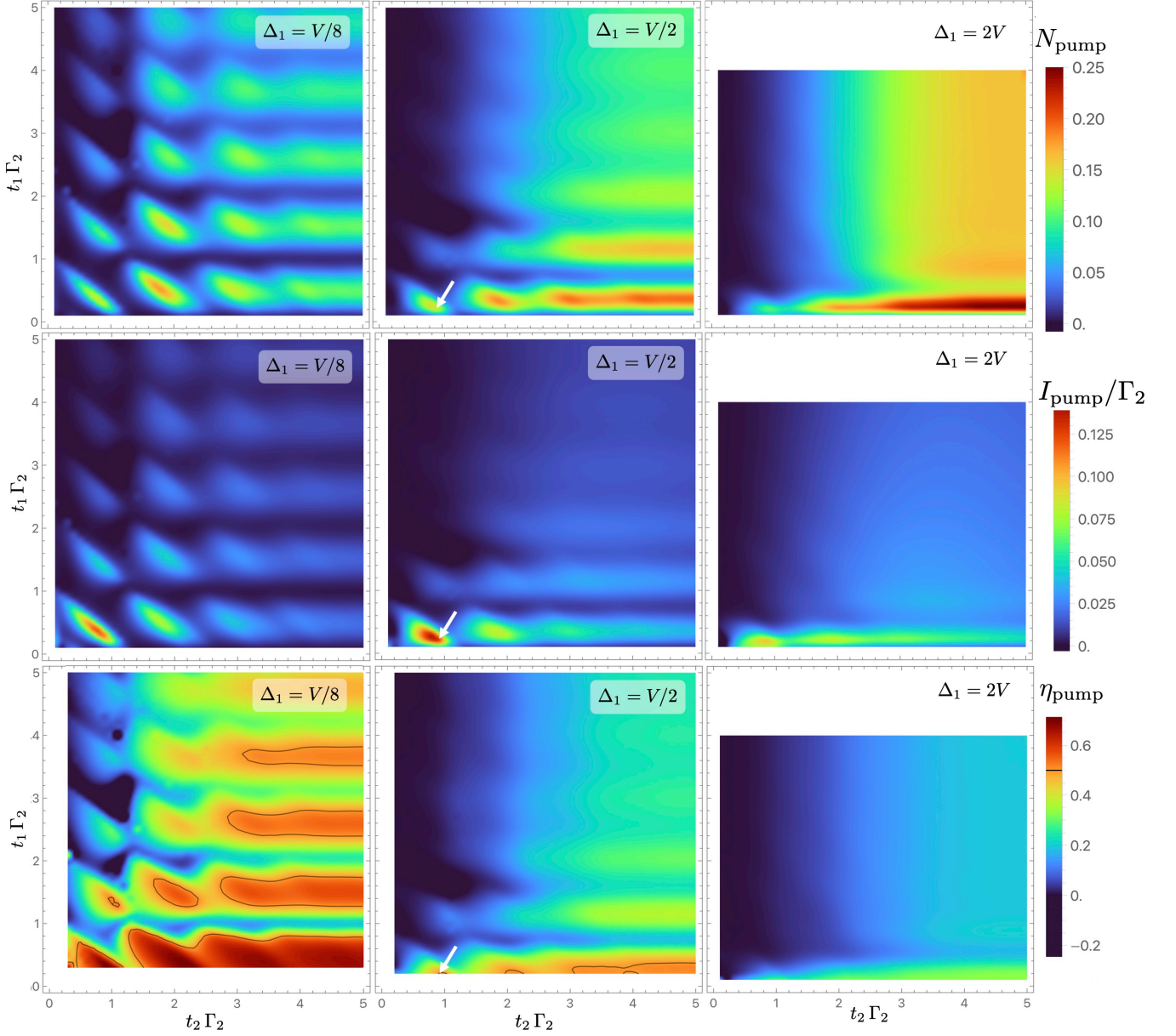


FIG. 9. The colors show the averaged number of pumped electrons N_{pump} (top-row), the current through the QD I_{pump} (middle-row) and the energy efficiency η_{pump} (bottom-row) as functions of the duration t_2 of step 2 and the duration t_1 of step 1. All three quantities show non-Markovian oscillations. In particular, these effects lead to an increase of the energy efficiency, η_{pump} , above the upper bound, $\eta_{\text{pump}} = \frac{1}{2}$, of the slow pumping regime, indicated by black contour lines. The coupling with the first bath is given by $\Gamma_1 = \frac{5}{2}V$ and the coupling with the second bath is given by $\Gamma_2 = \frac{V}{8}$. The peak position of the spectral coupling-density of the first bath is given by $\omega_1 = 0$ and the width varies with each column ($\Delta_1 = \frac{V}{8}$, $\Delta_1 = \frac{V}{2}$, $\Delta_1 = 2V$). In contrast to this, the peak position of the spectral coupling-density of the second bath is located at the QD-orbital energy $\omega_2 = \varepsilon = \frac{5}{4}V$ and the width is given by $\Delta_2 = \frac{V}{4}$. The white arrow corresponds to the situation shown in Figure 10. For numerical reasons, we compute $N_{\text{pump}} \approx N_{\text{pump},10}$, $I_{\text{pump}} \approx I_{\text{pump},10}$ and $\eta_{\text{pump}} \approx \eta_{\text{pump},10}$ for the tenth cycle and assume that this is identical to the limit cycle. However, this assumption is not valid for η_{pump} , small $t_1 + t_2$ and small Δ_1 in particular. Therefore, the plots for η_{pump} have an adjusted and restricted plot range. For $\Delta_1 = 2V$, there is a restricted plot range for all quantities because of computational reasons.

1 to the QD via

$$I_{1 \rightarrow \text{QD}} = -2\sqrt{\frac{\Gamma_1 \Delta_1}{2}} \text{Im} \langle r_1^\dagger c \rangle. \quad (16)$$

In order to reach high energy efficiency, we use parameters ω_1 and Δ_1 in the lower left region of Figure 7. Moreover, we choose $\Gamma_2 \ll \Gamma_1$, $\omega_2 = \varepsilon$ and $\Delta_2 < \varepsilon - V$ to

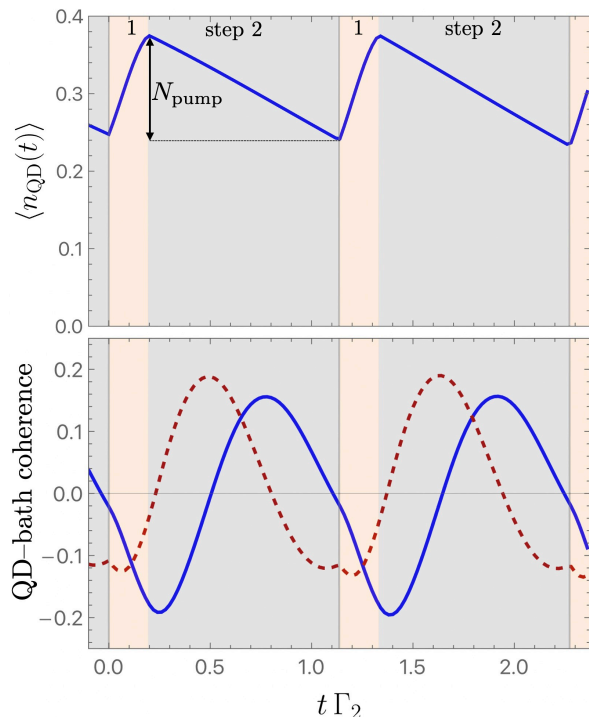


FIG. 10. The Figures show the particle number of the QD (top) and the coherence $\langle r_1^\dagger c \rangle$ (cf. Eq. (4)) (bottom: blue–solid curve $\hat{=}$ real part; red–dashed curve $\hat{=}$ imaginary part) as functions of time t . The durations of step 1 and step 2 are $t_1 = \frac{\pi}{2\sqrt{\varepsilon^2 + 2\Gamma_1\Delta_1}} \neq t_2 = \frac{3\pi}{2\varepsilon}$ and correspond to the white arrow in Figure 9. In contrast to Figure 8, t_2 is so short that $\langle r_1^\dagger c \rangle$ does not vanish during step 2. This leads to an increase of the current during step 1. In addition, t_1 is chosen such that the non–Markovian oscillations of the particle number lead to an improved value of N_{pump} . The other parameters are given by $\Gamma_1 = \frac{5}{2}V$, $\Delta_1 = \frac{V}{2}$, $\Gamma_2 = \frac{V}{4}$, $\Delta_2 = \frac{V}{8}$, $\varepsilon = \frac{5}{4}V$, $\omega_1 = 0$ and $\omega_2 = \varepsilon$.

suppress unwanted tunneling from the second bath to the QD. As before, we will use the exact solution discussed in Appendix A.

The top panel of Figure 8 displays the QD occupation number as a function of time. The orange and gray areas indicate step 1 and step 2, respectively. During step 1, the electrons coherently oscillate with frequency $\sqrt{\varepsilon^2 + 2\Gamma_1\Delta_1}$ between bath 1 and the QD for a short time. This is a consequence of the peaked bath structure. The amplitude of the oscillation decays with time, such that the QD occupation approaches the stationary QD occupation $\langle n_{\text{stat},1} \rangle$ (given by Eq. (10) in Section III A). For finite t_1 , the values of N_{pump} , I_{pump} , and also η_{pump} depend on whether the end of step 1 corresponds to a high or a low point of this oscillation.

The bottom panel of Figure 8 displays both the real and the imaginary part of the coherence between QD and bath 1 as a function of time. It is interesting to note that the coherence is not only present during step 1, in

which the QD is coupled to bath 1. There is finite (but decaying) coherence also during step 2. Since there is no tunneling coupling to bath 1 during step 2, the real and imaginary part of the QD–bath 1 coherence are not associated with a coupling energy or a charge transfer. Nevertheless, the decaying oscillations during step 2 do have an impact on pumping if t_2 is sufficiently small such that at the end of step 2 the coherence between QD and bath 1 has not yet fully vanished. Depending on whether the imaginary part has a high or low point at the end of step 2, a current flows directly from or to the QD at the beginning of the following step 1.

The influence of finite values of t_1 and t_2 is illustrated in Figure 9, which shows, at small times and small enough Δ_1 , pronounced oscillations of N_{pump} , I_{pump} , and η_{pump} as a function of t_1 and t_2 . Figure 10 shows an optimal situation where t_1 is chosen such that the first oscillation peak of the particle number corresponds to the end of step 1 and t_2 is chosen so that the imaginary part of the coherence between the first bath and the QD has a low point at the end of step 2. These parameters correspond to an enhanced I_{pump} , as indicated with a white arrow in Figure 9.

With increasing Δ_1 , the oscillations of the coherences between the baths and the QD decay faster and, finally, become invisible in N_{pump} , I_{pump} , and η_{pump} . A large energy efficiency η_{pump} is achieved for small Δ_1 , for which oscillations are pronounced, by properly choosing t_2 . On the one hand, the efficiency also increases as N_{pump} increases due to a large negative value of the imaginary part of the coherence at the end of step 2. On the other hand, efficiency increases as the work performed decreases due to a large positive value of the real part of the coherence at the end of step 2. This interplay leads to the relative shift between the maxima of N_{pump} and η_{pump} , as shown in Figure 9, the latter partially exceeding $\frac{1}{2}$. For further discussion, in particular on how the energy efficiency is limited by bath excitations, see Appendix B.

As a result, non–Markovian effects can increase the efficiency with which the work performed by coupling and decoupling is converted into the chemical energy gain of the second bath. Moreover, the presence of oscillations of N_{pump} , I_{pump} and η_{pump} as functions of t_1 and t_2 is an indicator that coherences and the coupling energy play an important role. For this, it is essential that t_1 and t_2 are chosen accurately, where the tolerance range is smaller than $1/\sqrt{\varepsilon^2 + 2\Gamma_1\Delta_1}$ for t_1 and smaller than $1/\varepsilon$ for t_2 .

IV. PUMPING SCHEME 2

Similar to the first pumping scheme, also the second one relies on using the coupling energy between quantum dot (QD) and baths through decoherence processes. In pumping scheme 1, the decoherence is triggered by decoupling the QD from the bath. This requires a time–dependent variation of the tunnel couplings. In pumping scheme 2, decoherence is invoked by measuring the QD

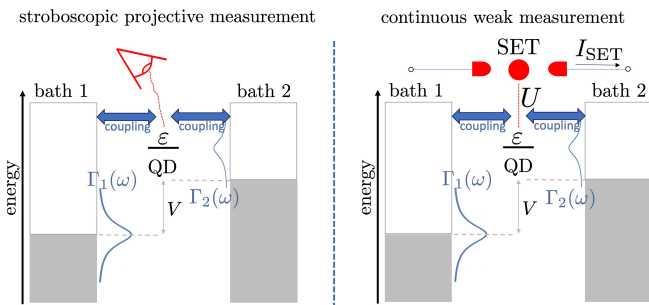


FIG. 11. Schematic visualization of the functionality of the second pumping scheme discussed in Section IV: In contrast to the electron pump shown in Figure 3, here both baths are always coupled to the QD. Stroboscopic projective measurements (left) or a continuous and weak measurement via a single-electron transistor (SET) with interaction U and current I_{SET} (right) are applied to the QD. For appropriately chosen spectral densities $\Gamma_1(\omega)$, $\Gamma_2(\omega)$ the measurements induce electron transport from bath 1 to bath 2.

occupation.

This measurement-induced pumping mechanism bears similarities to the anti-Zeno effect [41–44] and to a contemporaneous study for a similar device in [74].

In contrast to the first pumping scheme, we will now consider a setup in which both baths are always coupled to the QD ($g_\nu(t) \equiv 1, \nu = 1, 2$ in Eq. (3)), where the structure of the baths determines a preferred direction of the tunneling. Decoherence occurs by coupling a charge detector to the QD. This could be done in various ways. Here, we discuss two limiting cases, see Figure 11. In the first scenario, a strong, i.e., projective measurement is performed in a stroboscopic manner — see left panel of Figure 11. This scheme, discussed in Section IV A, has the conceptual advantage that the decoherence occurs at well-defined, externally controlled instants in time. The second scenario, described in Section IV B, relies on a continuous and weak measurement — see right panel of Figure 11. Such steady-state situation may be easier to implement experimentally.

A. Stroboscopic projective measurement

If both baths stay coupled to the QD and no measurements are performed, the applied bias voltage V will drive, via higher-order tunneling processes, a constant current⁷ I_{stat} from bath 2 to bath 1. This can, however, change in presence of measurements. A projective measurement of the QD particle number and averaging over all measurement outcomes modifies the density matrix by only deleting the coherences between the QD and

⁷ This is related to the strict positivity of the entropy production rate, $dS/dt = \beta(\mu_1 - \mu_2)I_{\text{stat}} > 0$, [80].

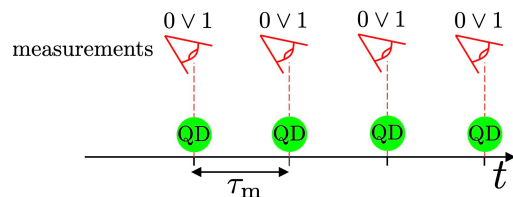


FIG. 12. Schematic visualization of the measurement scheme discussed in Section IV A as a function of time t . The measurements of the particle number of the QD (0 or 1) are repeated stroboscopically with the time interval τ_m .

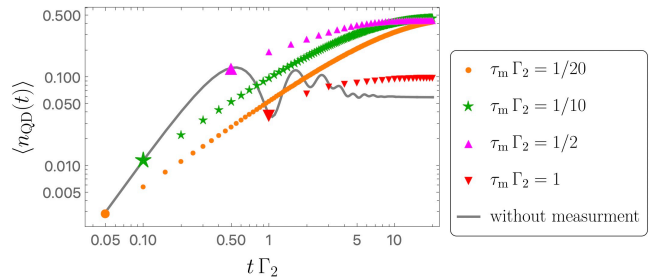


FIG. 13. The expectation value of the QD occupation $\langle n_{\text{QD}} \rangle$ as a function of the time t that has elapsed since the QD was in the empty initial state (double logarithmic scale): The solid curve shows $\langle n_{\text{QD}} \rangle$ without repeated measurements, whereas the symbols show $\langle n_{\text{QD}} \rangle$ for periodically repeated measurements with τ_m and averaged over all results of the measurements. For $t \rightarrow \infty$, $\langle n_{\text{QD}} \rangle$ becomes stationary with as well as without measurements. The stationary $\langle n_{\text{QD}} \rangle$ with measurements are larger than without measurements. In contrast, the rapidity with which $\langle n_{\text{QD}} \rangle$ converges toward its stationary value is slowed down for short measurement intervals τ_m (Zeno-effect [81]). For the calculations, we use the exact solution discussed in Appendix C 1. The parameters are given by $\omega_1 = 0$, $\omega_2 = \varepsilon = \frac{5}{4}V$, $\Gamma_1 = \frac{5}{2}V$, $\Gamma_2 = \frac{V}{4}$ and $\Delta_1 = \Delta_2 = \frac{V}{8}$.

the baths⁸ (cf. Appendix C 1 for the exact description). At early times after the measurement, the electrons may enter the QD even if $\varepsilon > V$, involving the rebuild of coherences between the baths and the QD. However, these processes are suppressed for later times when the coherences become stationary. For measurements that are repeated stroboscopically with time interval τ_m (cf. Figure 12), the QD can gain energy from the system-bath coupling for short times after each measurement [28] (deletion of the coherences) which results in a higher final occupation number of the QD than without the repeated measurements (cf. Figure 13). This effect is similar to the anti-Zeno effect [41–44]⁹.

⁸ However, the coherences between the baths and the coherences inside the baths remain unaffected.

⁹ But also the Zeno effect [81] is present for short τ_m and t (cf. Figure 13).

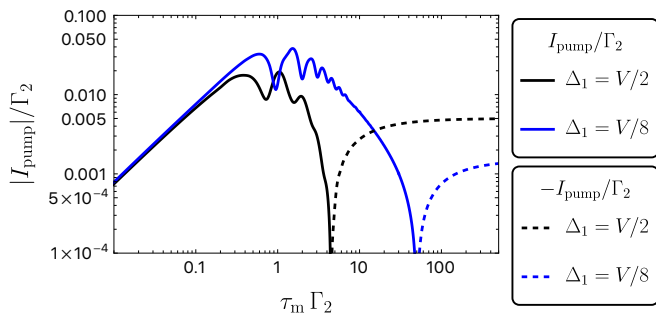


FIG. 14. The averaged current I_{pump} , induced by periodically repeated measurements, is shown as a function of the measurement interval τ_m (in units of the coupling strength Γ_2 between the QD and bath 2) for two different values $\Delta_1 = \frac{V}{8}$ (blue) and $\Delta_1 = \frac{V}{2}$ (black) in a double logarithmic scale. It increases linearly for short τ_m (Zeno regime), equally for both values of Δ_1 , since the weak coupling between the QD and the second bath becomes the common limiting factor. Later, there appear oscillations corresponding to electrons oscillating between the first bath and the QD. For large τ_m , the averaged current decays as $1/\tau_m$ against the stationary current $I_{\text{stat}} < 0$ without measurements, where a negative I_{pump} is indicated by a dashed curve and its absolute value increases with increasing Δ_ν . The other parameters are $\omega_1 = 0$, $\omega_2 = \varepsilon = \frac{5}{4}V$, $\Gamma_1 = \frac{5}{2}V$, $\Gamma_2 = \frac{V}{4}$, $\Delta_2 = \frac{V}{8}$. The exact solution discussed in Appendix C 1 is used for the calculations.

A proper choice of the spectral densities¹⁰ $\Gamma_1(\omega)$ and $\Gamma_2(\omega)$ (with strong coupling to occupied states of bath 1 and coupling to mainly unoccupied states of bath 2, respectively) may lead to an electric current flowing against V : from bath 1 to bath 2. The required energy is obtained from the measurement process¹¹. Figure 14 shows the current averaged over the pumping cycle

$$\begin{aligned} I_{\text{pump}} &= \frac{1}{\tau_m} \lim_{\ell \rightarrow \infty} \int_{(\ell-1)\tau_m}^{\ell\tau_m} dt I_{1 \rightarrow \text{QD}}(t) \\ &= -\frac{1}{\tau_m} \lim_{\ell \rightarrow \infty} \int_{(\ell-1)\tau_m}^{\ell\tau_m} dt I_{2 \rightarrow \text{QD}}(t) \end{aligned} \quad (17)$$

(cf. Eq. (16)) as a function of the measurement interval τ_m . In the limit of infinitely frequent measurements ($\tau_m \rightarrow 0$), I_{pump} vanishes because the measurements always delete the coherences between the QD and the baths, thus stopping any dynamics, which is known as the Zeno effect [81]. Specifically, the current between the baths and the QD increases linearly in time t starting from zero directly after each measurement. As a consequence, also the averaged current I_{pump} increases linearly

with the interval τ_m for short τ_m . However, the current between the baths and the QD deviates from the linear behavior for later times, when oscillations between the baths and the QD become relevant. This can be observed as oscillations in the averaged current (cf. Figure 14)¹². After the energy injected by the measurement process is used up, there is no pumping against the bias anymore in that cycle. The averaged current then decays as $1/\tau_m$ against the negative stationary current $I_{\text{stat}} < 0$ from bath 2 to bath 1. The impact of the higher-order tunneling processes enabling I_{stat} increases as Δ_ν increases (cf. black and blue curves in Figure 14).

B. Continuous weak measurement

The realization of a stroboscopic strong measurement scheme requires a higher degree of control than just permanently coupling a charge detector to the QD, which continuously performs a weak measurement. As we show in this section, a continuous weak measurement can be sufficient to establish measurement-induced pumping. For this, we consider a single-electron transistor (SET) that is capacitively coupled to the QD. Such setups are sometimes [83, 84] used to measure the occupation of the QD and the shot noise of the additional channel can induce drag or ratchet currents [67, 70, 85] through the QD. This is modeled by the total Hamiltonian

$$\begin{aligned} H' &= H + U n_{\text{SET}} c^\dagger c + \sum_{\nu,k} \left(\gamma_{\text{SET}} b_{\nu,k}^\dagger c_{\text{SET}} + \text{h.c.} \right) \\ &\quad + \sum_{\nu,k} \varepsilon_{\nu,k} b_{\nu,k}^\dagger b_{\nu,k} \end{aligned} \quad (18)$$

where we add an additional QD with fermionic annihilation and creation operators $c_{\text{SET}}/c_{\text{SET}}^\dagger$ (and $n_{\text{SET}} = c_{\text{SET}}^\dagger c_{\text{SET}}$) to the Hamiltonian H (cf. Eq. (1) and Eq. (3) with $g_\nu(t) = 1$). This QD interacts with the original QD via Coulomb interaction U and is connected to two baths $\nu = \text{source, drain}$ (of the SET) with fermionic annihilation/creation operators $b_{\nu,k}/b_{\nu,k}^\dagger$. The chemical potentials of the baths are chosen as $\mu_{\text{source}} = U/2$, $\mu_{\text{drain}} < 0$, so that the lowest-order tunneling processes only permit a current between the source and the drain if the original QD is unoccupied. Therefore, the current flowing through the SET can be interpreted as a continuous measurement of the particle number of the original QD. Compared to τ_m for projective measurements, here, the average time τ_e between two consecutive electrons flowing through the SET indicates the strength of the measurement. That time is given by the inverse of the average

¹⁰ One possibility of generating structured baths is to add additional QDs between the original QD and the baths, as discussed in Section II B for the reaction-coordinate mapping.

¹¹ The energy efficiency η_{pump} can be calculated similarly to Eq. (14). However, in reality, infinite work ($\eta_{\text{pump}} \rightarrow 0$) needs to be performed to realize an ideal projective measurement [82].

¹² These oscillations are similar to the oscillations (as a function of t_1) for the coupling/decoupling procedure (cf. Section III B).

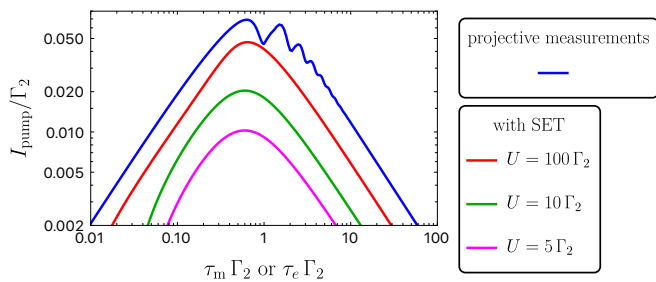


FIG. 15. The averaged current I_{pump} induced by periodically repeated measurements (blue) or the SET (other colors) is shown as a function of the measurement interval τ_m (blue) or the average time between two consecutive electrons flowing through the SET $\tau_e = 1/I_{\text{SET}}$ (other colors) in units of the coupling strength Γ_2 between the QD and bath 2 (double logarithmic scale). Here, the results are calculated with the Redfield equation in combination with the reaction-coordinate mapping (cf. Appendix D). The Redfield solution for the periodically repeated measurements differs from the exact solution discussed in Figure 14. In particular, the Redfield equation prevents off-resonant tunneling processes from bath 2 to bath 1 that are present for the exact solution and cause negative currents in Figure 14. Thus, we are in a regime where the Redfield solution cannot be applied quantitatively, but still shows qualitative agreement with the exact solution. The currents for the SET show a similar behavior as for the projective measurements but show no oscillations and vanish for $U \rightarrow 0$. The parameters are given by $\omega_1 = 0$, $\omega_2 = \varepsilon = \frac{5}{4}V$, $\Gamma_1 = \frac{5}{2}V$, $\Gamma_2 = \frac{V}{4}$, $\Delta_2 = \frac{V}{8}$ and $\Delta_1 = \frac{V}{8}$.

current¹³ flowing through the SET, $\tau_e = 1/I_{\text{SET}}$.

Figure 15 shows the averaged current I_{pump} induced by projective measurements (blue curve) and the SET (other colors) as a function of τ_m or $\tau_e = 1/I_{\text{SET}}$. For calculations we use the Redfield equation in combination with fermionic reaction-coordinate mapping (cf. Appendix D). The curves corresponding to the situation with SET are similar to those of the projective measurements. The reason is the noise from the electron tunneling through the SET which causes the QD energy level to fluctuate between ε and $\varepsilon + U$. It is known [72] that random fluctuations of the energy level of the QD lead to decoherence between the QD and the baths, which has a similar effect as the deletion of the coherences after the projective measurement¹⁴. However, the decay of

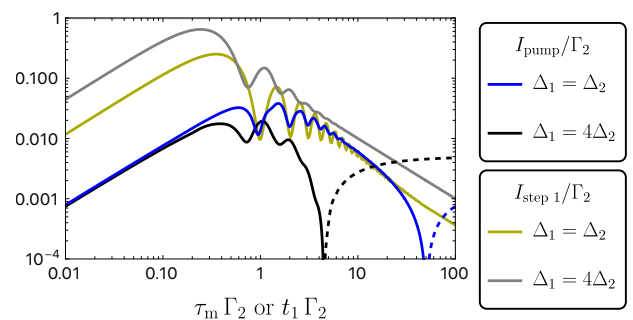


FIG. 16. The averaged current I_{pump} induced by projective measurements (cf. Figure 14) and the current $I_{\text{step 1}}$ (cf. Eq. (19) and Section III B) as functions of the measuring interval τ_m or the duration t_1 of step 1 (in units of the coupling strength Γ_2 between the QD and bath 2). Negative values are indicated by dashed curves. The parameters are given by $t_2 \rightarrow \infty$, $\omega_1 = 0$, $\omega_2 = \varepsilon = \frac{5}{4}V$, $\Gamma_1 = \frac{5}{2}V$, $\Gamma_2 = \frac{V}{4}$, $\Delta_2 = \frac{V}{8}$ and $\Delta_1 = \frac{V}{8}$ or $\Delta_1 = \frac{V}{2}$.

the coherence, which corresponds to a fluctuation, is not instantaneous for finite U , so the measurement induced I_{pump} is suppressed compared to the projective measurements and vanishes as $\sim U^2$ for small U . In addition, the capacitive coupling U blocks the current flow in the case when the SET is occupied and therefore I_{pump} stays smaller than for the projective measurements, even in the limit $U \rightarrow \infty$. Furthermore, the time interval between the entry of two electrons into the SET is not constant, so the oscillations of I_{pump} average out, contrary to the periodically repeated projective measurements.

V. COMPARISON OF THE TWO PUMPING SCHEMES

In the above sections, we have seen that it is possible to pump electrons by using a coupling/decoupling procedure (cf. Section III) as well as by performing measurements of the QD occupation (cf. Section IV). In both cases, the pumping processes are related to externally induced decoherence operations (cf. Figure 1). Although the exact realization of these operations differ from each other, it is possible to compare the results of the two pumping schemes not only qualitatively but also quantitatively.

For this, we consider the coupling/decoupling scheme (scheme 1) in the limit $t_2 \rightarrow \infty$. Then, there will be a total decay of the coherences between the QD and bath 1 during step 2. Consequently, at the beginning of step 1 there will be no coherences between the QD and bath 1, similar to the situation after a projective measurement. In contrast, after the measurement (scheme 2), there always remain some coherences between different bath modes which influence the dynamics (cf. Appendix C 2). Figure 16 compares the averaged current I_{pump} for

¹³ The average time between two consecutive electrons flowing through the SET can be defined by $\tau_e \equiv \lim_{t \rightarrow \infty} t/N_{\text{SET}}(t) = 1/I_{\text{SET}}$, where $N_{\text{SET}}(t)$ is the number of electrons flowing through the SET during the time interval t .

¹⁴ In contrast to [72], we consider a situation where fluctuations in the energy level of the QD are not completely random because, in our case, the occupations of the QD and the SET influence each other.

Our situation is similar to [74] or to the drag current discussed in [70], where the main effect results from shot noise-induced decoherence.

the projective measurements with the averaged current

$$I_{\text{step 1}} = \frac{N_{\text{pump}}}{t_1} \quad (19)$$

during step 1 for the coupling/decoupling procedure. The two currents show qualitatively similar behavior for both pumping schemes. Moreover, for $\Delta_1 = \Delta_2$ (blue and dark yellow), the frequency and phase of the oscillations coincide quantitatively for moderate durations ($\tau_m, t_1 \in [1/\Gamma_2, 10/\Gamma_2]$)¹⁵. For longer durations (up to $t_1, \tau_m = 30/\Gamma_2$), the corresponding currents are also quantitatively the same. However, for the pumping scheme with measurements, there is always a coupling between both baths and the QD, by which I_{pump} becomes negative for long durations, while in the coupling/decoupling procedure there is only a coupling between bath 1 and the QD during step 1, hence $I_{\text{step 1}}$ stays always positive. For short durations, both average currents show a linear behavior where I_{pump} is limited by the weak coupling between the QD and the second bath (cf. Section IV A), while $I_{\text{step 1}}$ is limited by the strong coupling between the QD and the first bath and is about $\frac{\Gamma_1 \Delta_1}{\Gamma_2 \Delta_2}$ times larger¹⁶ than I_{pump} .

VI. CONCLUSIONS

In this work, we studied the influence of off-resonant tunneling and the related impact of the QD-bath coupling on the electron transport through quantum dots (QDs). We have focused on two electron pumps that pump electrons against an applied voltage and operate only in the higher-order tunneling regime. Both types of pumps consist of a single-level QD coupled to two fermionic baths at zero temperature and operate by decoherence operations and the corresponding resets of the coupling energy which drive off-resonant tunneling events.

In pumping scheme 1, we applied a coupling and decoupling procedure. It turned out that very structured baths may increase the efficiency with which the coupling/decoupling work is converted into the chemical energy gain of the second bath. Furthermore, finite cycle durations of the pumping procedure lead to strong non-Markovian effects, which correspond to oscillating electron occupations and coherences, and we used these to further increase efficiency. In addition, the presence of these oscillations is a clear signature for the importance

of coherences between the QD and the bath for the involved processes.

In pumping scheme 2, we considered a similar situation as before, but with periodically repeated projective measurements of the QD occupation and static couplings between the QD and the baths. For properly chosen bath structures and sufficiently frequent measurements, the measurements generate a current against the voltage applied between the baths. In addition, we showed that even a weak continuous measurement by a charge detector, simulated by a single-electron transistor, can be sufficient to generate these currents. For both measurement realizations, the energy required for the pumping is gained by the measurements through the reset of the coupling energy and coherences between the QD and the baths for each measurement or during the continuous measurement and is similar to the anti-Zeno effect. Although the procedure is different, similar non-Markovian effects are observed as in the first pumping scheme and there is qualitative and quantitative agreement in the current flow between both schemes because both are driven by analogous decoherence operations and the manipulation of the coupling energy.

ACKNOWLEDGMENTS

The authors thank Johann Zöllner for fruitful discussions and valuable feedback on the manuscript. We gratefully acknowledge funding by the Deutsche Forschungsgemeinschaft (DFG, German Research Foundation) — Project 278162697 — SFB 1242.

Appendix A: Exact solution for time-dependent systems

1. Exact solution

In this section, we will extend the Heisenberg equation and the Laplace transform technique [77] to time-dependent Hamiltonians and we will reach an exact solution that has previously been derived by other methods [62, 66]. With Eq. (A11) and Eq. (A12) below it is possible to calculate the time dependence of all relevant expectation values.

We start with considering a total Hamiltonian

$$H(t) = \tilde{H}_S(t) + \sum_{k,\nu} \varepsilon_{\nu,k} a_{\nu,k}^\dagger a_{\nu,k} + \sum_{k,\nu} (t_{\nu,k} a_{\nu,k}^\dagger c_\nu + \text{h.c.}) \quad (\text{A1})$$

with time-independent tunneling matrix elements $t_{\nu,k}$ that satisfy the wideband limit. We note that, in this general formulation, each level ν of the system (with fermionic annihilation operator c_ν) may be coupled to its own bath (with fermionic annihilation operators $a_{\nu,k}$). In

¹⁵ For $\Delta_1 \neq \Delta_2$, $I_{\text{step 1}}$ scales with Δ_1/Δ_2 .

¹⁶ Immediately after a measurement (Zeno regime) or at the begin of step 1, the current between the QD and the reaction coordinate of bath ν increases linearly with time t and behaves like $\sim \lambda_\nu^2 t$ with $\lambda_\nu = \sqrt{\Gamma_\nu \Delta_\nu/2}$, respectively. The ratio of the slopes corresponding to baths 1 and 2 is then $\frac{\lambda_1^2}{\lambda_2^2} = \frac{\Gamma_1 \Delta_1}{\Gamma_2 \Delta_2}$.

contrast to [77], we allow the Hermitian system Hamiltonian $\tilde{H}_S(t)$ to be time dependent. The Heisenberg equations of motion for the annihilation operators are given by

$$\partial_t c_{\nu,H}(t) = i[\tilde{H}_{S,H}(t), c_{\nu,H}(t)] - i \sum_k t_{\nu,k}^* a_{\nu,k,H}(t) \quad (\text{A2})$$

and

$$\partial_t a_{\nu,k,H}(t) = -i\varepsilon_{\nu,k} a_{\nu,k,H}(t) - it_{\nu,k} c_{\nu,H}(t) \quad (\text{A3})$$

with $\partial_t \equiv \frac{d}{dt}$. The index H indicates that the operator is in the Heisenberg picture $A_H(t) = U^\dagger(t)A(t)U(t)$ with the time evolution operator $U(t)$ obeying the differential equation $\partial_t U(t) = -iH(t)U(t)$. The Laplace transformation, $\mathcal{L}[g(t)](z) = \int_0^\infty dt g(t)e^{-zt}$, of Eqs. (A2), (A3) gives

$$\mathcal{L}[\partial_t c_{\nu,H}(t)](z) = i\mathcal{L}[\tilde{H}_{S,H}(t), c_{\nu,H}(t)](z) - i \sum_k t_{\nu,k}^* \mathcal{L}[a_{\nu,k,H}(t)](z) \quad (\text{A4})$$

and

$$\mathcal{L}[a_{\nu,k,H}(t)](z) = \frac{a_{\nu,k} - it_{\nu,k} \mathcal{L}[c_{\nu,H}(t)](z)}{z + i\varepsilon_{\nu,k}}. \quad (\text{A5})$$

In Eq. (A5), we have used the mathematical relation $\mathcal{L}[\partial_t a_{\nu,k,H}(t)](z) = z\mathcal{L}[a_{\nu,k,H}(t)](z) - a_{\nu,k,H}(0)$ and the fact that $a_{\nu,k,H}(0) = a_{\nu,k}$ refers back to the Schrödinger picture.

Next, we insert Eq. (A5) into Eq. (A4). Thereby, we encounter the sum

$$A(z) := \sum_k \frac{|t_{\nu,k}|^2}{z + i\varepsilon_{\nu,k}} = \int_{-\infty}^{\infty} \frac{d\omega}{2\pi} \frac{\Gamma_\nu(\omega)}{z + i\omega} \quad (\text{A6})$$

with $\Gamma_\nu(\omega) = 2\pi \sum_k |t_{\nu,k}|^2 \delta(\varepsilon_{\nu,k} - \omega)$. In the wideband limit, i.e., for an energy-independent spectral-coupling density $\Gamma_\nu(\omega) \equiv \Gamma_\nu$, Eq. (A6) simplifies to the z -independent constant $A = \Gamma_\nu/2$. This yields

$$\mathcal{L}[\partial_t c_{\nu,H}(t)](z) = i\mathcal{L}[\tilde{H}_{S,H}(t), c_{\nu,H}(t)](z) - \frac{\Gamma_\nu}{2} \mathcal{L}[c_{\nu,H}(t)](z) - i \sum_k \frac{t_{\nu,k}^* a_{\nu,k}}{z + i\varepsilon_{\nu,k}}. \quad (\text{A7})$$

Since (as a consequence of the wideband limit) z appears explicitly only in the last term, we can easily perform the inverse Laplace transformation. We arrive at

$$\partial_t c_{\nu,H}(t) = i[H_{\text{eff},H}(t), c_{\nu,H}(t)] - i \sum_k t_{\nu,k}^* e^{-i\varepsilon_{\nu,k}t} a_{\nu,k} \quad (\text{A8})$$

with an effective non-Hermitian operator

$$H_{\text{eff}}(t) = \tilde{H}_S(t) - i \sum_\nu \frac{\Gamma_\nu}{2} c_\nu^\dagger c_\nu \quad (\text{A9})$$

in the Schrödinger and $H_{\text{eff},H}(t) = U^\dagger(t)H_{\text{eff}}(t)U(t)$ in the Heisenberg picture.

If $\tilde{H}_S(t)$ is bilinear in c_ν and c_ν^\dagger with $\nu = 1, \dots, N$, Eq. (A8) can be explicitly written as

$$\partial_t \begin{pmatrix} c_{1,H}(t) \\ c_{2,H}(t) \\ \vdots \\ c_{N,H}(t) \end{pmatrix} = \mathbf{M}(t) \begin{pmatrix} c_{1,H}(t) \\ c_{2,H}(t) \\ \vdots \\ c_{N,H}(t) \end{pmatrix} - i \sum_k \begin{pmatrix} t_{1,k}^* e^{-i\varepsilon_{1,k}t} a_{1,k} \\ t_{2,k}^* e^{-i\varepsilon_{2,k}t} a_{2,k} \\ \vdots \\ t_{N,k}^* e^{-i\varepsilon_{N,k}t} a_{N,k} \end{pmatrix} \quad (\text{A10})$$

where the time-dependent $N \times N$ matrix $\mathbf{M}(t)$ is derived from the commutators in Eq. (A8). The solution of the differential equation is

$$\begin{pmatrix} c_{1,H}(t) \\ c_{2,H}(t) \\ \vdots \\ c_{N,H}(t) \end{pmatrix} = \mathbf{O}(t) \begin{pmatrix} c_1 \\ c_2 \\ \vdots \\ c_N \end{pmatrix} - i\mathbf{O}(t) \int_0^t ds \sum_k \mathbf{O}^{-1}(s) \begin{pmatrix} t_{1,k}^* e^{-i\varepsilon_{1,k}s} a_{1,k} \\ t_{2,k}^* e^{-i\varepsilon_{2,k}s} a_{2,k} \\ \vdots \\ t_{N,k}^* e^{-i\varepsilon_{N,k}s} a_{N,k} \end{pmatrix} \quad (\text{A11})$$

with the propagator $\mathbf{O}(t)$ obeying $\partial_t \mathbf{O}(t) = \mathbf{M}(t)\mathbf{O}(t)$, with $\mathbf{O}(0) = 1$.

This exact solution is only applicable to situations with time-independent $t_{\nu,k}$ in the wideband limit ($\Delta \rightarrow \infty$). In order to use this technique for our studies as well, we employ the fermionic reaction-coordinate mapping as described in Section II B. For this, $\mathbf{M}(t)$ is given by the 3×3 matrix

$$\mathbf{M}(t) = - \begin{pmatrix} i\varepsilon & 0 & 0 \\ 0 & \Delta_1 + i\omega_1 & 0 \\ 0 & 0 & \Delta_2 + i\omega_2 \end{pmatrix} - g_1(t) \sqrt{\frac{\Gamma_1 \Delta_1}{2}} \begin{pmatrix} 0 & i & 0 \\ i & 0 & 0 \\ 0 & 0 & 0 \end{pmatrix} - g_2(t) \sqrt{\frac{\Gamma_2 \Delta_2}{2}} \begin{pmatrix} 0 & 0 & i \\ 0 & 0 & 0 \\ i & 0 & 0 \end{pmatrix}, \quad (\text{A12})$$

where the first row/column refer to the QD level ($c_1 \equiv c$), the second to reaction-coordinate 1 ($c_2 \equiv r_1$) and the third to reaction-coordinate 2 ($c_3 \equiv r_2$). The fact that, after the mapping, the QD orbital is no longer coupled to the bath is accounted for by setting $t_{1,k} = 0$. The coupling of reaction-coordinate 1 and 2 to their respective bath, $t_{2,k} \equiv \tilde{\gamma}_{1,k}$ and $t_{3,k} \equiv \tilde{\gamma}_{2,k}$ with $a_{2,k} \equiv \tilde{a}_{1,k}$ and $a_{3,k} \equiv \tilde{a}_{2,k}$, leads to the (transformed) spectral-coupling

density $\tilde{\Gamma}_\nu(\omega) = 2\pi \sum_k |\tilde{\gamma}_{\nu,k}|^2 \delta(\omega - \tilde{\varepsilon}_{\nu,k}) = 2\Delta_\nu$, which satisfies the wideband condition. The imaginary parts of $\mathbf{M}(t)$ represent the energy levels of $\tilde{H}_S(t)$, while the real parts of $\mathbf{M}(t)$ correspond to the decay rates and the effective broadening of the energy levels due to higher-orders in the tunnel coupling.

With Eq. (A11) and Eq. (A12), we know the creation/annihilation operators in the Heisenberg picture as a function of time and the operators in the Schrödinger picture, and we are able to calculate the time dependence of the expectation values of all observables for given initial conditions.

2. Stationary QD occupation

From Eq. (A11) and Eq. (A12) it follows

$$\langle n_{\text{stat},\nu} \rangle = \int_{-\infty}^{\infty} \frac{d\omega}{2\pi} \frac{\Gamma_\nu f_+(\omega, \mu_\nu)}{(\varepsilon - \omega)^2 + \left(\frac{\Gamma_\nu}{2} + \frac{(\varepsilon - \omega)(\omega - \mu_\nu)}{\Delta_\nu} \right)^2} \quad (\text{A13})$$

for the stationary QD occupation at the end of each step $\nu = 1, 2$ for $t_1, t_2 \rightarrow \infty$ (cf. Section III A). The coupling strength Γ_ν and the width Δ_ν are given by the original $\Gamma(\omega, t)$ (cf. Eq. (3)). The function $f_+(\omega, \mu_\nu) = 1/[e^{\beta(\omega - \mu_\nu)} + 1]$ is the Fermi function for the inverse temperature β , chemical potentials μ_ν and energy ω . If Γ_1 is sufficiently large compared to Γ_2 , it is possible to end up with $\langle n_{\text{stat},1} \rangle > \langle n_{\text{stat},2} \rangle$ even though $\mu_2 > \mu_1$.

3. Energetic efficiency calculated via the ground states of $\tilde{H}_S(t)$

In the following we consider the slow pumping regime of pumping scheme 1 discussed in Section III A for $\Gamma_2 \ll \varepsilon - V$ and $\Gamma_2 \ll \Gamma_1$. For $\omega_1 \leq \frac{\Gamma_1 \Delta_1}{2}$, the number of pumped electrons N_{pump} and the coupling/decoupling work can be calculated by approximating the stationary states with the ground states of $\tilde{H}_S(t)$ (cf. Eq. (6)). It results in

$$\eta_{\text{pump}} \approx \frac{V}{\varepsilon - \omega_1 + \sqrt{(\varepsilon - \omega_1)^2 + 2\Gamma_1 \Delta_1}} \quad (\text{A14})$$

for $0 \leq \omega_1 \leq \frac{\Gamma_1 \Delta_1}{2}$. For $\varepsilon \searrow V$, the efficiency reaches the maximum value $\eta_{\text{pump}} = \frac{1}{2}$ in the limit $\omega_1 \nearrow \frac{\Gamma_1 \Delta_1}{2}$ or in the limit $\Delta_1 \Gamma_1 \rightarrow 0$ for $\omega_1 = 0$.

Appendix B: Influence of bath excitations on the energy efficiency of pumping

1. Bath vs quantum-dot excitations

In this appendix, we discuss the energy efficiency of pumping scheme 1 in the regime of extremely weak cou-

pling Γ_2 between the QD and the second bath ($\Gamma_2 \ll \varepsilon - V \ll V$ and $\Gamma_2 \ll \Gamma_1$) and long durations of the second step (formally $t_2 \rightarrow \infty$). In this regime, the work $W_C(t_1)$ (cf. Eq. (13)) performed by the coupling/decoupling procedure changes the energy $\Delta E_{\text{QD}} = \varepsilon n_{\text{QD}}(t_1)$ of the QD and bath 1 (ΔE_B), while the bath 2 remains unaffected. Then, the energy efficiency

$$\eta_{\text{pump}} \approx \frac{\varepsilon n_{\text{QD}}(t_1)}{W_C(t_1)} = \frac{\Delta E_{\text{QD}}}{\Delta E_B + \Delta E_{\text{QD}}} \quad (\text{B1})$$

quantifies the energy gain of the QD (ΔE_{QD}), used for pumping, as a part of the total work $W_C(t_1) = \Delta E_B + \Delta E_{\text{QD}}$, while the energy excitations of the bath (ΔE_B) do not contribute to pumping. The energy efficiency is, therefore, traced back to how the performed work is distributed between QD and bath.

To resolve the bath degrees of freedom further, we introduce the energy gain density

$$\Delta E_B(\omega) = \sum_k \varepsilon_{1,k} \left[\langle n_{1,k}(t_1) \rangle - \langle n_{1,k}(0) \rangle \right] \delta(\varepsilon_{1,k} - \omega) \quad (\text{B2})$$

that describes the gain in mode ω of the bath and consider separately the part of the bath states below the Fermi level

$$\Delta E_{B,<0} = \int_{-\infty}^0 d\omega \Delta E_B(\omega) \quad (\text{B3})$$

and above the Fermi level

$$\Delta E_{B,>0} = \int_0^{\infty} d\omega \Delta E_B(\omega), \quad (\text{B4})$$

which add up to the total energy gain of bath, $\Delta E_B = \Delta E_{B,<0} + \Delta E_{B,>0}$.

Figure 17 shows the different contributions ΔE_{QD} , $\Delta E_{B,<0}$, $\Delta E_{B,>0}$, and ΔE_B as functions of the duration t_1 . Technical details of the calculations are provided in the next subsection. For short t_1 , the number of electrons leaving the bath, here $n_{\text{QD}}(t_1) = \Delta E_{\text{QD}}/\varepsilon$, increases quadratically with t_1 ,

$$n_{\text{QD}}(t_1) \sim t_1^2 \quad (\text{for } t_1 \sqrt{\Gamma_1 \Delta_1/2} \ll 1). \quad (\text{B5})$$

In combination with

$$\Delta E_{B,<0} = -\bar{\varepsilon}(t_1) n_{\text{QD}}(t_1) \quad (\text{B6})$$

and the averaged energy of the leaving electrons, $\bar{\varepsilon}(t_1) \sim \log t_1 < 0$, it follows that $\Delta E_{B,<0} \sim -t_1^2 \log t_1$. Excitations to states above the Fermi level are only possible by including the QD as an intermediate step, and the corresponding energy $\Delta E_{B,>0} \sim -t_1^4 \log t_1$ increases slower than $\Delta E_{B,<0}$ for short t_1 . Therefore, $\Delta E_{B,<0}$ dominates in this regime and the efficiency is given by

$$\eta_{\text{pump}} \approx \frac{\varepsilon}{\varepsilon - \bar{\varepsilon}(t_1)} \quad (\text{B7})$$

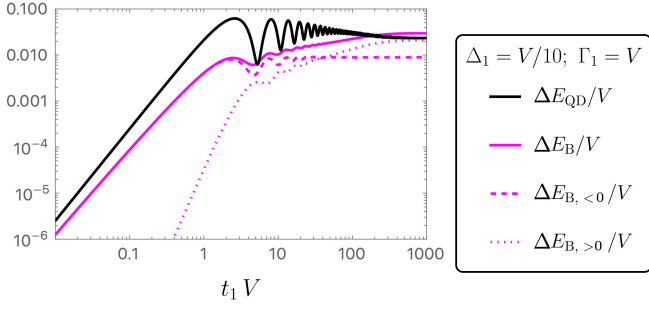


FIG. 17. The energy gain ΔE_{QD} of the QD and of the bath $\Delta E_{\text{B}} = \Delta E_{\text{B},<0} + \Delta E_{\text{B},>0}$ during step 1 are shown as functions of the duration t_1 of step 1. The energy gain of the bath is the sum of the energy gain $\Delta E_{\text{B},<0}$ induced by electrons that leave the bath from states below the Fermi level and the energy gain $\Delta E_{\text{B},>0}$ induced by electrons that enter the bath to states above the Fermi level. For short t_1 , ΔE_{QD} behaves like $\sim t_1^2$ and $\Delta E_{\text{B},<0}$ behaves approximately like $\sim t_1^2 \log t_1$. In contrast to this, $\Delta E_{\text{B},>0}$ behaves like $\sim t_1^4 \log t_1$. The parameters are $\Delta_1 = V/10$, $\Gamma_1 = V$, $\omega_1 = 0$, $\Gamma_2 \ll \varepsilon - V \ll V$, $\Gamma_2 \ll \Gamma_1$ and $t_2 \rightarrow \infty$.

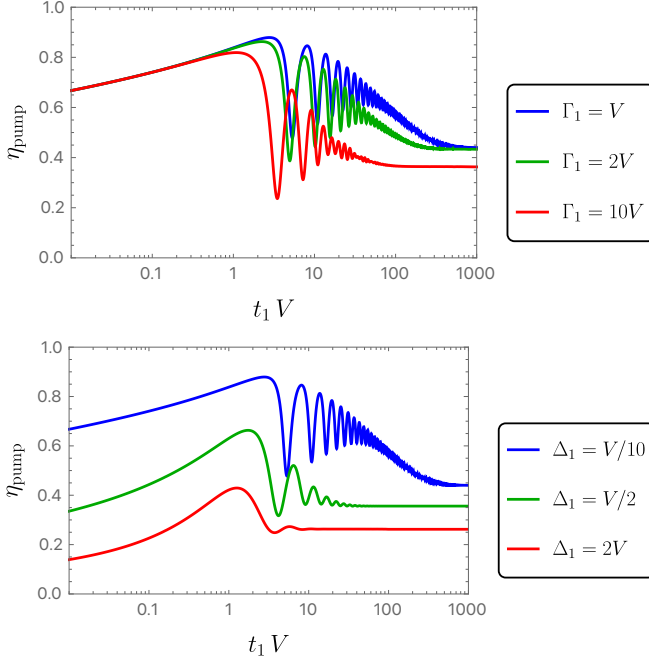


FIG. 18. The energy efficiency η_{pump} (top and bottom) is shown as a function of the duration t_1 of step 1. The parameters are $\omega_1 = 0$, $\Gamma_2 \ll \varepsilon - V \ll V$, $\Gamma_2 \ll \Gamma_1$ and $t_2 \rightarrow \infty$. Top: The different curves correspond to different Γ_1 but identical $\Delta_1 = V/10$. Bottom: The different curves correspond to different Δ_1 but identical $\Gamma_1 = V$.

where $\bar{\varepsilon}(t_1)$ depends only on Δ_1 and t_1 and, hence, η_{pump} becomes independent of Γ_1 (cf. Figure 18 — top). For long t_1 , electrons entering the QD above the Fermi level (corresponding to $\Delta E_{\text{B},>0}$) become relevant and lead to a reduction of η_{eff} compared to short t_1 where the reduction increases with increasing Γ_1 or Δ_1 (Figure 18).

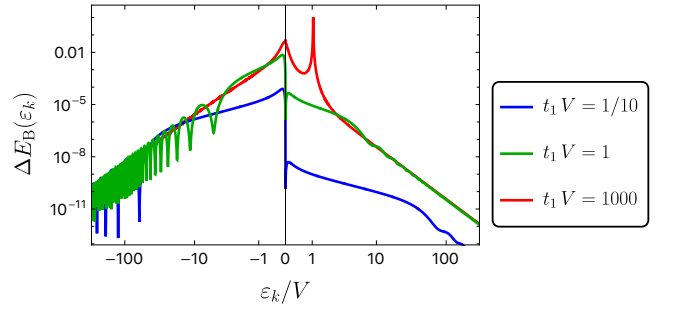


FIG. 19. The energy density $\Delta E_{\text{B}}(\varepsilon_k)$ (cf. Eq. (B2)) corresponding to the change in bath energy during step 1 is shown as a function of ε_k for three different values of t_1 . The vertical axis is scaled logarithmically and the horizontal axis is scaled with $\text{arsinh}(\cdot)$, resulting in a double-log plot for $|\varepsilon_k|/V \gg 1$. The parameters are the same as in Figure 17.

Figure 19 shows $\Delta E_{\text{B}}(\varepsilon_k)$ as a function of the energy ε_k of the corresponding bath mode for different durations t_1 . For long t_1 , $\Delta E_{\text{B}}(\varepsilon_k)$ is localized at the Fermi level and at the energy level of the QD. The peak, corresponding to the energy level of the QD, vanishes for smaller t_1 when $\Delta E_{\text{B},>0}$ is not dominant. The flanks of $\Delta E_{\text{B}}(\varepsilon_k)$ decay as $\sim |\varepsilon_k|^{-3}$. In a range of approximately $|\varepsilon_k| \lesssim \frac{1}{t_1}$, the flanks show a suppressed decay $\sim |\varepsilon_k|^{-1}$ for short t_1 . This flattening leads to the time dependence of $\bar{\varepsilon}(t_1)$ and η_{pump} for short t_1 (cf. Eq. (B6) and Eq. (B7)).

2. Calculation details

For $\Gamma_2 \ll \varepsilon - V \ll V$, $\Gamma_2 \ll \Gamma_1$ and $t_2 \rightarrow \infty$, the density matrix ρ_0 of the model universe at the beginning of step 1 is a product state between the ground state¹⁷ of bath 1 and the state of an empty QD. In this case, it would be an unnecessary complication to use Eq. (A11) together with Eq. (A12) after a reaction-coordinate mapping, since in terms of the transformed degrees of freedom the initial state is no longer a product state. Instead, we repeat the procedure for deriving the exact solution presented in Appendix A 1, but this time assuming a time-independent system Hamiltonian (since the tunnel couplings are kept constant during the steps), while taking into account the Lorentzian-shaped spectral coupling density for the coupling between QD and bath 1. Up to Eqs. (A4) and (A5), the derivation remains the same with only one system degree of freedom, $\nu = 1$. For Eq. (A4), we use the relation $\mathcal{L}[\partial_t c_{1,\text{H}}(t)](z) = z\mathcal{L}[c_{1,\text{H}}(t)](z) - c_1$ and explicitly calculate the commutator $[\tilde{H}_{\text{S,H}}(t), c_{1,\text{H}}(t)] = -\varepsilon c_{1,\text{H}}(t)$. The

¹⁷ This means $\text{tr}(\rho_0 a_{1,k}^\dagger a_{1,q}) = \delta_{k,q} \Theta(-\varepsilon_{1,k})$ and this is not identical to $\text{tr}(\rho_0 \tilde{a}_{1,k}^\dagger \tilde{a}_{1,q}) = \delta_{k,q} \Theta(-\tilde{\varepsilon}_{1,k})$ (cf. Section II B).

sum in Eq. (A6), that appears when inserting Eq. (A5) into Eq. (A4), preserves its z dependence,

$$A(z) = \frac{1}{2} \frac{\Gamma_1 \Delta_1}{z + i\omega_1 + \Delta_1}, \quad (\text{B8})$$

and is, in contrast to the wideband limit, no longer constant. As a result, we have to replace Eq. (A7) by

$$\mathcal{L}[c_{1,H}(t)](z) = \frac{1}{z + i\varepsilon + \frac{1}{2} \frac{\Gamma_1 \Delta_1}{z + i\omega_1 + \Delta_1}} \left(c_1 - i \sum_k \frac{\gamma_{1,k}^* a_{1,k}}{z + i\varepsilon_{1,k}} \right). \quad (\text{B9})$$

It is now straightforward to perform the inverse Laplace transformation on Eq. (B9) and Eq. (A5) to get $a_{1,k,H}(t)$ and $c_{1,H}(t)$ as functions of t , c_1 and $a_{1,k}$. With this, we are able to calculate the time dependence of the particle number of the QD $\langle n_{\text{QD}}(t) \rangle = \text{tr}(\rho_0 c_{1,H}^\dagger(t) c_{1,H}(t))$ and of the bath states $\langle n_{1,k}(t) \rangle = \text{tr}(\rho_0 a_{1,k,H}^\dagger(t) a_{1,k,H}(t))$ by using $\text{tr}(\rho_0 c_1^\dagger c_1) = \text{tr}(\rho_0 c_1^\dagger a_{1,k}) = 0$ and $\text{tr}(\rho_0 a_{1,k}^\dagger a_{1,q}) = \delta_{k,q} \Theta(-\varepsilon_{1,k})$. Here, the occupation $\langle n_{1,k}(t) \rangle$ of each mode k changes only by a small value in time and vanishes in the continuum limit. However, the sum over all bath states leads to a finite change in the number of particles in the bath.

Appendix C: Stroboscopic projective measurement

1. Implementation

A projective measurement of the particle number of the QD with measurement outcome n_i is given by the superoperator \mathcal{P}_n that maps the density matrix ρ onto

$$\mathcal{P}_n[\rho] = \frac{P_n \rho P_n}{p_n}. \quad (\text{C1})$$

Here, $P_0 = cc^\dagger$ is the projector for the measurement outcome “0”, $P_1 = c^\dagger c$ the projector for the measurement outcome “1”, and

$$p_n = \text{tr}(P_n \rho) \quad (\text{C2})$$

is the probability to measure the QD occupation n . Averaging over all measurement outcomes leads to the density matrix

$$\bar{\rho} = \sum_n p_n \mathcal{P}_n[\rho] = P_0 \rho P_0 + P_1 \rho P_1. \quad (\text{C3})$$

In consequence, each measurement deletes coherences between the QD and the baths. However, the coherences between the baths and the coherences inside the baths remain unaffected. This point will be illustrated in Appendix C 2.

The immediate destruction of the coherence between QD and bath due to a projective measurement is implemented into the exact–solution scheme described in

Appendix A 1 with the following trick. We formally introduce two copies of the QD orbital, described by the annihilation operators c_1 and c_2 . Before the measurement, only orbital 1 is coupled to the baths, while orbital 2 is uncoupled. The measurement process is modeled by decoupling orbital 1 and, at the same time, coupling orbital 2 to the (same) baths and using the initial condition that orbital 2 has the same occupation as orbital 1, $\langle c_2^\dagger c_2 \rangle = \langle c_1^\dagger c_1 \rangle$, at the time of measurement. In that way, the information about the QD occupation is transferred from the first to the second copy of the orbital, but the coherences between QD and baths are lost. In contrast, coherences within the baths remain. The fact, that such coherences can have measurable effects is demonstrated in the next subsection.

Now we know how to implement one projective measurement into the exact–solution scheme. For more than one measurement, the discussed trick can be repeated with the number of required QD copies given by the number of measurements.

2. Effect of intra–bath coherences

To illustrate the relevance of coherences within the baths (intra–bath coherences), we consider in this subsection a simple case scenario where a QD is in equilibrium with one bath with a wideband spectral coupling density, $\Delta \rightarrow \infty$. The equilibrium condition implies that, on average, there is no current flowing between QD and bath. The average QD occupation is some number between 0 and 1. After a projective measurement, the QD occupation is either $n = 0$ or $n = 1$. In the subsequent time evolution, the QD occupation reaches again its average value, i.e., current is flowing transiently between QD and bath. The detailed time dependence of this current depends on whether intra–bath coherences are taken into account or not.

This is illustrated in Figure 20, which shows the time derivative of the particle number of the QD (i.e., the current) as a function of time after having measured n by a projective measurement (dashed curves). This is compared to the case when bath is assumed to be in an equilibrium Gibbs state with no intra–bath coherences (solid curves). We find that there are significant deviations between the initially correlated and the initially uncorrelated bath. For the chosen parameters, for which the QD is more likely to be occupied than empty, the deviations are more pronounced for $n = 0$.

To understand on a formal level that the intra–bath coherences can matter, we calculate the time derivative of the current operator $\hat{I}_k = i \sum_k \left(\gamma_k a_k^\dagger c - \text{h.c.} \right)$ between the bath mode k and the QD. Making use of

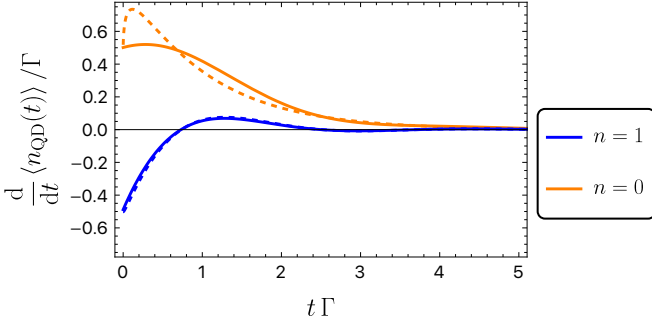


FIG. 20. The total current is shown as a function of time. For the dashed curves, the initial state is prepared by measuring the occupation of the QD. In contrast, the solid curves indicate the situation where the initial state of the bath is given by a state where no coherences between different bath modes are present. For an initially unoccupied QD (orange color), there are significant differences between the total currents of the two different bath states, whereas for an initially occupied QD (blue color), the total currents for the two different prepared initial states are similar. The parameters are $\varepsilon = \mu - 2\Gamma$ are $\Delta \rightarrow \infty$ (wideband).

$\frac{d\hat{I}_k}{dt} = i[H, \hat{I}_k]$, we obtain

$$\begin{aligned} \frac{d\hat{I}_k}{dt} = & 2|\gamma_k|^2 (a_k^\dagger a_k - c^\dagger c) + (\varepsilon - \varepsilon_k) (\gamma_k a_k^\dagger c + \text{h.c.}) \\ & + \sum_{l \neq k} (\gamma_k^* \gamma_l a_l^\dagger a_k + \text{h.c.}) . \end{aligned} \quad (\text{C4})$$

The first term, that depends on the occupation difference between QD and bath, is not affected by coherences. The second term corresponds to coherences between QD and bath that are destroyed by the projective measurement. The third term, however, corresponds to coherences between different bath modes. As a consequence, these coherences can influence the time derivative of the current and, thus, the current itself.

Appendix D: Continuous weak measurement

The setup for pumping scheme 2 with continuous weak measurement is described by the Hamiltonian Eq. (18). After performing the reaction-coordinate mapping for the QD (but not the SET), we have to deal with the system, described by the Hamiltonian

$$\begin{aligned} H'_S = & Un n_{\text{SET}} + \varepsilon n + \sum_{\nu} \omega_{\nu} r_{\nu}^{\dagger} r_{\nu} \\ & + \sum_{\nu} \sqrt{\frac{\Gamma_{\nu} \Delta_{\nu}}{2}} (r_{\nu}^{\dagger} c + \text{h.c.}) \end{aligned} \quad (\text{D1})$$

with $n = c^\dagger c$ the occupation of the QD and the occupation n_{SET} of the SET. The tunnel couplings of the reaction coordinates to the baths are described by the tunneling

strengths $2\Delta_{\nu}$, and the SET orbital is coupled to its baths with strength Γ_{SET} . All these couplings are given in the wideband limit.

Due to the interaction term $Un n_{\text{SET}}$, which is quartic in the fermionic operators, the exact solution following the procedure described in Appendix A 1 is no longer available. Therefore, we employ for this part, as an alternative, a systematic perturbation expansion in the tunnel couplings. For this, we derive a master equation for the reduced density matrix ρ_S of system S by integrating out the degrees of freedom of the baths and neglect terms beyond the first order in Γ_{SET} and Δ_{ν} . The result is the Redfield-II equation [28, 86, 87]

$$\begin{aligned} \partial_t \rho_S(t) = & -i [H'_S + H'_{S,\text{Lamb}}, \rho_S(t)] \\ & + \sum_{\alpha, \nu} \sum_{\Delta E, \Delta E'} \frac{f_{\alpha}(\Delta E, \mu_{\nu}) + f_{\alpha}(\Delta E', \mu_{\nu})}{2} \\ & \times \left(K_{\nu}^{\alpha}(\Delta E) \rho_S(t) K_{\nu}^{\alpha}(\Delta E')^{\dagger} \right. \\ & \left. - \frac{1}{2} \{ K_{\nu}^{\alpha}(\Delta E')^{\dagger} K_{\nu}^{\alpha}(\Delta E), \rho_S(t) \} \right) \end{aligned} \quad (\text{D2})$$

with $\nu \in \{1, 2, \text{source}, \text{drain}\}$, $\alpha \in \{\pm\}$, the renormalization (or Lamb-shift) term¹⁸

$$\begin{aligned} H'_{S,\text{Lamb}} = & i \sum_{\nu, \alpha} \frac{f_{\alpha}(\Delta E', \mu_{\nu}) - f_{\alpha}(\Delta E, \mu_{\nu})}{4} \\ & \times K_{\nu}^{\alpha}(\Delta E')^{\dagger} K_{\nu}^{\alpha}(\Delta E) \end{aligned} \quad (\text{D3})$$

and the jump operators

$$K_{\nu}^{\pm}(\Delta E) = \sqrt{2\Delta_{\nu}} \sum_{k,l} \delta_{E_k - E_l, \pm \Delta E} |E_k\rangle \langle E_k| r_{\nu}^{\pm} |E_l\rangle \langle E_l| \quad (\text{D4})$$

for $\nu = 1, 2$ and

$$K_{\nu}^{\pm}(\Delta E) = \sqrt{\Gamma_{\text{SET}}} \sum_{k,l} \delta_{E_k - E_l, \pm \Delta E} |E_k\rangle \langle E_k| c_{\text{SET}}^{\pm} |E_l\rangle \langle E_l| \quad (\text{D5})$$

for $\nu = \text{source}, \text{drain}$. Here, $f_{+}(\Delta E, \mu_{\nu}) = 1/[e^{\beta(\Delta E - \mu_{\nu})} + 1]$ is the Fermi function, in our case at zero temperature ($\beta \rightarrow \infty$), and $f_{-}(\Delta E, \mu_{\nu}) = 1 - f_{+}(\Delta E, \mu_{\nu})$. The states $|E_l\rangle$ are eigenstates of H'_S with eigenenergies E_l .

We use Eq. (D2) to find the stationary state $\rho_{S,\text{stat}}$ and calculate the pumped current

$$I_{\text{pump}} = -2\sqrt{\frac{\Gamma_1 \Delta_1}{2}} \text{Im} \langle r_1^{\dagger} c \rangle = 2\sqrt{\frac{\Gamma_2 \Delta_2}{2}} \text{Im} \langle r_2^{\dagger} c \rangle \quad (\text{D6})$$

¹⁸ Here, we neglect the imaginary prefactors in Eq. (D2) and the real prefactors of the renormalized term in Eq. (D3) for simplicity [28].

and the current flowing through the SET

$$I_{\text{SET}} = \langle \mathcal{D}_{\text{source}} n_{\text{SET}} \rangle = - \langle \mathcal{D}_{\text{drain}} n_{\text{SET}} \rangle \quad (\text{D7})$$

with

$$\begin{aligned} \mathcal{D}_\nu n_{\text{SET}} = & \sum_\alpha \sum_{\Delta E, \Delta E'} \frac{f_\alpha(\Delta E, \mu_\nu) + f_\alpha(\Delta E', \mu_\nu)}{2} \\ & \times \left(K_\nu^\alpha(\Delta E)^\dagger n_{\text{SET}} K_\nu^\alpha(\Delta E') \right. \\ & \left. - \frac{1}{2} \{ K_\nu^\alpha(\Delta E')^\dagger K_\nu^\alpha(\Delta E), n_{\text{SET}} \} \right). \quad (\text{D8}) \end{aligned}$$

In Figure 15, we vary Γ_{SET} and calculate I_{SET} and I_{pump} . When calculating $\rho_{\text{S,stat}}$ it is important to take the renormalization term $H'_{\text{S,Lamb}}$ into account. Otherwise, there appear nonphysical currents between the SET and the QD, unrelated to any tunneling term in the Hamiltonian H'_S . Moreover, the Redfield equation is only an approximation for small Δ_ν and small Γ_{SET} which leads to some errors, in particular, I_{pump} cannot become negative in the Redfield equation, while the exact solution enables negative currents. It breaks down for large Δ_ν or Γ_{SET} .

-
- [1] D. Newman, F. Mintert, and A. Nazir, Performance of a quantum heat engine at strong reservoir coupling, *Phys. Rev. E* **95**, 032139 (2017).
- [2] M. Wiedmann, J. T. Stockburger, and J. Ankerhold, Non-Markovian dynamics of a quantum heat engine: Out-of-equilibrium operation and thermal coupling control, *New J. Phys.* **22**, 033007 (2020).
- [3] P. A. Camati, J. F. G. Santos, and R. M. Serra, Employing Non-Markovian effects to improve the performance of a quantum Otto refrigerator, *Phys. Rev. A* **102**, 012217 (2020).
- [4] Y. Shirai, K. Hashimoto, R. Tezuka, C. Uchiyama, and N. Hatano, Non-Markovian effect on quantum Otto engine: Role of system-reservoir interaction, *Phys. Rev. Res.* **3**, 023078 (2021).
- [5] M. Ishizaki, N. Hatano, and H. Tajima, Switching the function of the quantum Otto cycle in Non-Markovian dynamics: Heat engine, heater, and heat pump, *Phys. Rev. Res.* **5**, 023066 (2023).
- [6] A. Das and V. Mukherjee, Quantum-enhanced finite-time Otto cycle, *Phys. Rev. Res.* **2**, 033083 (2020).
- [7] V. Mukherjee, A. G. Kofman, and G. Kurizki, Anti-Zeno quantum advantage in fast-driven heat machines, *Commun. Phys.* **3**, 8 (2020).
- [8] M. Xu, J. Stockburger, G. Kurizki, and J. Ankerhold, Minimal quantum thermal machine in a bandgap environment: Non-Markovian features and anti-Zeno advantage, *New J. Phys.* **24**, 035003 (2022).
- [9] K. Ptaszyński, Non-Markovian thermal operations boosting the performance of quantum heat engines, *Phys. Rev. E* **106**, 014114 (2022).
- [10] I. A. Picatoste, A. Colla, and H.-P. Breuer, Dynamically emergent quantum thermodynamics: Non-Markovian Otto cycle, *Phys. Rev. Res.* **6**, 013258 (2024).
- [11] J. Liu, K. A. Jung, and D. Segal, Periodically driven quantum thermal machines from warming up to limit cycle, *Phys. Rev. Lett.* **127**, 200602 (2021).
- [12] C. L. Latune, G. Pleasance, and F. Petruccione, Cyclic quantum engines enhanced by strong bath coupling, *Phys. Rev. Appl.* **20**, 024038 (2023).
- [13] S. P. Katoorani, C. Kohlfürst, F. Queisser, G. Schaller, and R. Schützhold, Finite-time performance of a cyclic two-dimensional quantum Ising heat engine, *Phys. Rev. E* **112**, 014122 (2025).
- [14] S. Gatto, A. Colla, H.-P. Breuer, and M. Thoss, Quantum Otto cycle in the Anderson impurity model (2026), arXiv:2601.21546 [cond-mat].
- [15] A. Ghosh, V. Mukherjee, W. Niedenzu, and G. Kurizki, Are quantum thermodynamic machines better than their classical counterparts?, *Eur. Phys. J.* **227**, 2043 (2019).
- [16] S. Restrepo, S. Böhling, J. Cerrillo, and G. Schaller, Electron pumping in the strong coupling and Non-Markovian regime: A reaction coordinate mapping approach, *Phys. Rev. B* **100**, 035109 (2019).
- [17] A. A. S. Kalae, A. Wacker, and P. P. Potts, Violating the thermodynamic uncertainty relation in the three-level maser, *Phys. Rev. E* **104**, L012103 (2021).
- [18] F. Cavaliere, M. Carrega, G. De Filippis, V. Cataudella, G. Benenti, and M. Sasseti, Dynamical heat engines with Non-Markovian reservoirs, *Phys. Rev. Res.* **4**, 033233 (2022).
- [19] M. Alamo, F. Petiziol, and A. Eckardt, Minimal quantum heat pump based on high-frequency driving and Non-Markovianity, *Phys. Rev. E* **109**, 064121 (2024).
- [20] L. M. Cangemi, C. Bhadra, and A. Levy, Quantum engines and refrigerators, *Phys. Rep.* **1087**, 1 (2024).
- [21] L. Schulman and B. Gaveau, Ratcheting up energy by means of measurement, *Phys. Rev. Lett.* **97**, 240405 (2006).
- [22] N. Erez, G. Gordon, M. Nest, and G. Kurizki, Thermodynamic control by frequent quantum measurements, *Nature* **452**, 724 (2008).
- [23] M. Esposito, K. Lindenberg, and C. Van den Broeck, Entropy production as correlation between system and reservoir, *New J. Phys.* **12**, 013013 (2010).
- [24] M. Esposito, M. A. Ochoa, and M. Galperin, Nature of heat in strongly coupled open quantum systems, *Phys. Rev. B* **92**, 235440 (2015).
- [25] P. Strasberg, G. Schaller, T. Brandes, and M. Esposito, Quantum and information thermodynamics: A unifying framework based on repeated interactions, *Phys. Rev. X* **7**, 021003 (2017).
- [26] P. Strasberg and M. Esposito, Non-Markovianity and negative entropy production rates, *Phys. Rev. E* **99**, 012120 (2019).
- [27] A. Trushechkin, M. Merkli, J. Cresser, and J. Anders, Open quantum system dynamics and the mean force Gibbs state, *AQS* **4**, 10.1116/5.0073853 (2022).

- [28] L. Litzba, E. Kleinherbers, J. König, R. Schützhold, and N. Szpak, Effective time-dependent temperature for fermionic master equations beyond the Markov and the secular approximations, *Phys. Rev. B* **111**, 085103 (2025).
- [29] I. A. Picatoste, A. Colla, and H.-P. Breuer, Local and global approaches to the thermodynamics of pure decoherence processes in open quantum systems, *Phys. Rev. A* **112**, 022210 (2025).
- [30] A. Colla, B. Vacchini, and A. Smirne, Local energy assignment for two interacting quantum thermal reservoirs, *New J. Phys.* **27**, 124510 (2025).
- [31] M. Perarnau-Llobet, H. Wilming, A. Riera, R. Gallego, and J. Eisert, Strong coupling corrections in quantum thermodynamics, *Phys. Rev. Lett.* **120**, 120602 (2018).
- [32] D. Gelbwaser-Klimovsky, N. Erez, R. Alicki, and G. Kurizki, Work extraction via quantum nondemolition measurements of qubits in cavities: Non-Markovian effects, *Phys. Rev. A* **88**, 022112 (2013).
- [33] P. Strasberg, G. Schaller, N. Lambert, and T. Brandes, Nonequilibrium thermodynamics in the strong coupling and Non-Markovian regime based on a reaction coordinate mapping, *New J. Phys.* **18**, 073007 (2016).
- [34] G. Engelhardt and G. Schaller, Maxwell's demon in the quantum-Zeno regime and beyond, *New J. Phys.* **20**, 023011 (2018).
- [35] G. Schaller, J. Cerrillo, G. Engelhardt, and P. Strasberg, Electronic Maxwell demon in the coherent strong-coupling regime, *Phys. Rev. B* **97**, 195104 (2018).
- [36] C. Elouard, S. K. Manikandan, A. N. Jordan, and G. Haack, Revealing the fuel of a quantum continuous measurement-based refrigerator, *Phys. Rev. E* **113**, 014134 (2026).
- [37] K. Liu, M. Nakagawa, and M. Ueda, Maxwell's demon for quantum transport, *Phys. Rev. A* **113**, 022436 (2026).
- [38] R. A. Bustos-Marín and H. L. Calvo, Thermodynamics and steady state of quantum motors and pumps far from equilibrium, *Entropy* **21**, 824 (2019).
- [39] K. Korzekwa, M. Lostaglio, J. Oppenheim, and D. Jennings, The extraction of work from quantum coherence, *New J. Phys.* **18**, 023045 (2016).
- [40] W. Chen, S.-W. Han, X. Feng, and J. Feng, Work extraction from long-lived quantum coherence of a three-level system (2025), arXiv:2508.02614 [quant-ph].
- [41] A. Kofman and G. Kurizki, Acceleration of quantum decay processes by frequent observations, *Nature* **405**, 546 (2000).
- [42] P. Facchi, H. Nakazato, and S. Pascazio, From the quantum Zeno to the inverse quantum Zeno effect, *Phys. Rev. Lett.* **86**, 2699 (2001).
- [43] K. Fujii and K. Yamamoto, Anti-Zeno effect for quantum transport in disordered systems, *Phys. Rev. A* **82**, 042109 (2010).
- [44] N. Ahmadi-iaz, M. Geller, J. König, P. Kratzer, A. Lorke, G. Schaller, and R. Schützhold, Quantum Zeno manipulation of quantum dots, *Phys. Rev. Res.* **4**, L032045 (2022).
- [45] M. Switkes, C. M. Marcus, K. Campman, and A. C. Gosard, An adiabatic quantum electron pump, *Science* **283**, 1905 (1999).
- [46] Y. Ono and Y. Takahashi, Electron pump by a combined single-electron/field-effect-transistor structure, *Appl. Phys. Lett.* **82**, 1221 (2003).
- [47] M. D. Blumenthal, B. Kaestner, L. Li, S. Giblin, T. J. B. M. Janssen, M. Pepper, D. Anderson, G. Jones, and D. A. Ritchie, Gigahertz quantized charge pumping, *Nat. Phys.* **3**, 343 (2007).
- [48] B. Kaestner, V. Kashcheyevs, S. Amakawa, M. D. Blumenthal, L. Li, T. J. B. M. Janssen, G. Hein, K. Pierz, T. Weimann, U. Siegner, and H. W. Schumacher, Single-parameter nonadiabatic quantized charge pumping, *Phys. Rev. B* **77**, 153301 (2008).
- [49] S. P. Giblin, M. Kataoka, J. D. Fletcher, P. See, T. J. B. M. Janssen, J. P. Griffiths, G. A. C. Jones, I. Farrer, and D. A. Ritchie, Towards a quantum representation of the ampere using single electron pumps, *Nat. Commun.* **3**, 930 (2012).
- [50] L. Fricke, M. Wulf, B. Kaestner, F. Hohls, P. Mirovsky, B. Mackrodt, R. Dolata, T. Weimann, K. Pierz, U. Siegner, and H. W. Schumacher, Self-referenced single-electron quantized current source, *Phys. Rev. Lett.* **112**, 226803 (2014).
- [51] A. Rossi, T. Tanttu, K. Y. Tan, I. Iisakka, R. Zhao, K. W. Chan, G. C. Tettamanzi, S. Rogge, A. S. Dzurak, and M. Möttönen, An accurate single-electron pump based on a highly tunable silicon quantum dot, *Nano Lett.* **14**, 3405 (2014).
- [52] G. Yamahata, K. Nishiguchi, and A. Fujiwara, Gigahertz single-trap electron pumps in silicon, *Nat. Commun.* **5**, 5038 (2014).
- [53] B. Kaestner and V. Kashcheyevs, Non-adiabatic quantized charge pumping with tunable-barrier quantum dots: A review of current progress, *Rep. Prog. Phys.* **78**, 103901 (2015).
- [54] F. Stein, D. Drung, L. Fricke, H. Scherer, F. Hohls, C. Leicht, M. Götz, C. Krause, R. Behr, E. Pesel, K. Pierz, U. Siegner, F. J. Ahlers, and H. W. Schumacher, Validation of a quantized-current source with 0.2ppm uncertainty, *Appl. Phys. Lett.* **107**, 103501 (2015).
- [55] F. Stein, H. Scherer, T. Gerster, R. Behr, M. Götz, E. Pesel, C. Leicht, N. Ubbelohde, T. Weimann, K. Pierz, H. W. Schumacher, and F. Hohls, Robustness of single-electron pumps at sub-ppm current accuracy level, *Metrologia* **54**, S1 (2016).
- [56] J. van der Heijden, G. C. Tettamanzi, and S. Rogge, Dynamics of a single-atom electron pump, *Sci. Rep.* **7**, 44371 (2017).
- [57] H. Scherer and H. W. Schumacher, Single-electron pumps and quantum current metrology in the revised si, *Ann. Phys.* **531**, 1800371 (2019).
- [58] S. P. Giblin, A. Fujiwara, G. Yamahata, M.-H. Bae, N. Kim, A. Rossi, M. Möttönen, and M. Kataoka, Evidence for universality of tunable-barrier electron pumps, *Metrologia* **56**, 044004 (2019).
- [59] A. Rossi, N. W. Hendrickx, A. Sammak, M. Veldhorst, G. Scappucci, and M. Kataoka, Single-hole pump in germanium, *J. Phys. D: Appl. Phys.* **54**, 434001 (2021).
- [60] F. Hohls, V. Kashcheyevs, F. Stein, T. Wenz, B. Kaestner, and H. W. Schumacher, Controlling the error mechanism in a tunable-barrier nonadiabatic charge pump by dynamic gate compensation, *Phys. Rev. B* **105**, 205425 (2022).
- [61] A. Dash, S. Yianni, M. Feng, F. Hudson, A. Saraiva, A. S. Dzurak, and T. Tanttu, Silicon-charge-pump operation limit above and below liquid-helium temperature, *Phys. Rev. Appl.* **21**, 014040 (2024).
- [62] A.-P. Jauho, N. S. Wingreen, and Y. Meir, Time-dependent transport in interacting and noninteract-

- ing resonant-tunneling systems, *Phys. Rev. B* **50**, 5528 (1994).
- [63] J. Splettstoesser, M. Governale, J. König, and R. Fazio, Adiabatic pumping through a quantum dot with Coulomb interactions: A perturbation expansion in the tunnel coupling, *Phys. Rev. B* **74**, 085305 (2006).
- [64] A. Croy and U. Saalman, Nonadiabatic rectification and current reversal in electron pumps, *Phys. Rev. B* **86**, 035330 (2012).
- [65] R.-P. Riwar, J. Splettstoesser, and J. König, Zero-frequency noise in adiabatically driven interacting quantum systems, *Phys. Rev. B* **87**, 195407 (2013).
- [66] S. Gurvitz, Single-electron approach for time-dependent electron transport, *Phys. Scr.* **2015**, 014013 (2015).
- [67] R. Hussein and S. Kohler, Capacitively coupled nano conductors: Ratchet currents and exchange fluctuation relations, *Ann. Phys.* **527**, 610 (2015).
- [68] R. Hussein, S. Kohler, and F. Sols, Heat pump driven by the shot noise of a tunnel contact, *Physica E* **77**, 156 (2016).
- [69] A. Croy and U. Saalman, Full counting statistics of a nonadiabatic electron pump, *Phys. Rev. B* **93**, 165428 (2016).
- [70] J. S. Lim, D. Sánchez, and R. López, Engineering drag currents in Coulomb coupled quantum dots, *New J. Phys.* **20**, 023038 (2018).
- [71] E. Potanina, K. Brandner, and C. Flindt, Optimization of quantized charge pumping using full counting statistics, *Phys. Rev. B* **99**, 035437 (2019).
- [72] S. Gurvitz, Generalized Landauer formula for time-dependent potentials and noise-induced zero-bias dc current, *J. Phys. A-Math. Theor.* **52**, 175301 (2019).
- [73] B. Annby-Andersson, D. Bhattacharyya, P. Bakhshinezhad, D. Holst, G. De Sousa, C. Jarzynski, P. Samuelsson, and P. P. Potts, Maxwell's demon across the quantum-to-classical transition, *Phys. Rev. Res.* **6**, 043216 (2024).
- [74] R. Sánchez, A. N. Singh, A. N. Jordan, and B. Bhandari, Making the virtual real: Measurement-powered tunneling engines (2025), arXiv:2510.22394 [quant-ph].
- [75] É. Jussiau, L. Bresque, A. Auffèves, K. W. Murch, and A. N. Jordan, Many-body quantum vacuum fluctuation engines, *Phys. Rev. Res.* **5**, 033122 (2023).
- [76] P. Zedler, G. Schaller, G. Kiesslich, C. Emary, and T. Brandes, Weak-coupling approximations in Non-Markovian transport, *Phys. Rev. B* **80**, 045309 (2009).
- [77] G. E. Topp, T. Brandes, and G. Schaller, Steady-state thermodynamics of non-interacting transport beyond weak coupling, *Europhys. Lett.* **110**, 67003 (2015).
- [78] P. Strasberg, G. Schaller, T. L. Schmidt, and M. Esposito, Fermionic reaction coordinates and their application to an autonomous Maxwell demon in the strong-coupling regime, *Phys. Rev. B* **97**, 205405 (2018).
- [79] H.-P. Breuer, Foundations and measures of quantum non-Markovianity, *J. Phys. B* **45**, 154001 (2012).
- [80] G. Nenciu, Independent electron model for open quantum systems: Landauer-Büttiker formula and strict positivity of the entropy production, *J. Math. Phys.* **48**, 033302 (2007).
- [81] B. Misra and E. G. Sudarshan, The Zeno's paradox in quantum theory, *J. Math. Phys.* **18**, 756 (1977).
- [82] Y. Guryanova, N. Friis, and M. Huber, Ideal projective measurements have infinite resource costs, *Quantum* **4**, 222 (2020).
- [83] R. J. Schoelkopf, P. Wahlgren, A. A. Kozhevnikov, P. Delsing, and D. E. Prober, The radio-frequency single-electron transistor (RF-SET): A fast and ultrasensitive electrometer, *Science* **280**, 1238 (1998).
- [84] C. Barthel, M. Kjaergaard, J. Medford, M. Stopa, C. M. Marcus, M. P. Hanson, and A. C. Gossard, Fast sensing of double-dot charge arrangement and spin state with a radio-frequency sensor quantum dot, *Phys. Rev. B* **81**, 161308 (2010).
- [85] D. Bischoff, M. Eich, O. Zilberberg, C. Rössler, T. Ihn, and K. Ensslin, Measurement back-action in stacked graphene quantum dots, *Nano Lett.* **15**, 6003 (2015).
- [86] A. G. Redfield, On the theory of relaxation processes, *IBM J. Res. Dev.* **1**, 19 (1957).
- [87] N. Szpak, G. Schaller, R. Schützhold, and J. König, Relaxation to persistent currents in a Hubbard trimer coupled to fermionic baths, *Phys. Rev. B* **110**, 115131 (2024).